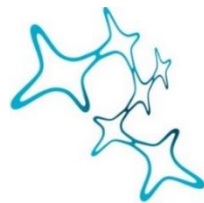


PERCEPTUAL DECISION MAKING IN LARVAL ZEBRAFISH REVEALED BY WHOLE-BRAIN IMAGING

Elena Ioana Dragomir



Graduate School of
Systemic Neurosciences
LMU Munich

Dissertation der Graduate School of Systemic Neurosciences
der Ludwig-Maximilians-Universität München

March 12th, 2019

Supervisor and First Reviewer: Dr. Ruben Portugues

Second Reviewer: Prof. Dr. Ilona Grunwald-Kadow

Third Reviewer: Dr. Isaac Bianco

Date of oral defense:
July 18th, 2019

Publication statement

The results presented in this PhD thesis were submitted for publication to the *Nature Neuroscience* journal, under the title “*Evidence accumulation during a perceptual decision task revealed by whole-brain imaging*”. The submission is currently under second round of review.

Most of the figures were taken from the manuscript, as were most of the methods sections, and parts of the results.

Abstract

Animals are able to accumulate sensory evidence over considerable timescales in order to select behaviors fundamental for their survival. Despite the importance and ubiquity of this phenomenon, how activity in different brain regions contributes to this process is not understood. In this study, I develop a novel perceptual decision making assay in the larval zebrafish, based on whole-field visual motion of varying strength. Upon presentation of motion, fish integrate this noisy sensory evidence in time before swimming in the direction of perceived motion, a behavior known as the optomotor response. Behavioral parameters such as the latency to initiate swimming and the fraction of correct turns are modulated by motion strength. Whole-brain functional imaging experiments with single-cell resolution enable identification of almost all neural activity relevant to the different stages of the decision making process, including evaluation of momentary sensory input, accumulation of this sensory evidence, and behavioral output. Fitting a generalized integrator model to every neuron reveals a wide range of time constants, which are distributed in functional clusters across different brain regions. Based on the behavior and the imaging data, a model is proposed where integrating units set the left and right turning rates. An unbiased whole-brain analysis revealed that the interpeduncular nucleus, a circular structure located ventrally on the midline of the brain, reliably encodes these rates.

Table of Contents

Abstract.....	v
1. Introduction.....	1
1.1 Perceptual decision making	1
1.1.1 Neural basis of perceptual decision making	2
1.1.2 Theoretical models describing decision processes	6
1.2 The larval zebrafish as a model organism in systems neuroscience	7
1.2.1 Zebrafish neuroanatomy	8
1.2.2 Optical tools for dissecting behavioral neural circuits.....	11
1.2.3 The zebrafish optomotor response	12
1.3 Thesis objectives	14
2. Materials and methods	16
2.1 Zebrafish husbandry.....	16
2.2 Freely-swimming behavioral experiments.....	16
2.2.1 Behavioral Setup.....	16
2.2.2 Visual motion stimulus	17
2.2.3 Stimulus protocol.....	19
2.2.4 Behavioral tracking.....	19
2.3 Head-restrained behavioral experiments.....	20
2.3.1 Behavioral setup.....	20
2.3.2 Visual motion stimulus	20
2.3.3 Stimulus protocol	21
2.3.4 Behavioral tracking and bout categorization	21
2.4 Whole-brain imaging experiments.....	22
2.4.1 Two-Photon Calcium Imaging setup and acquisition.....	22
2.4.2 Stimulus protocol.....	22
2.4.3 Image analysis.....	23
2.4.4 Anatomical registration.....	24
2.4.5 Regressors and correlation analysis	24

2.4.6 Computation of motor triggers.....	25
2.5 Model fitting	25
2.5.1 Logistic multivariate regression model.....	25
2.5.2 Generalized integrator model.....	26
2.5.3 Poisson model for generation of turns	27
2.5.4 Generation of synthetic freely-swimming behavior	28
3. Results	29
3.1 The optomotor response as a function of coherence.....	29
3.2 Effect of motion stimulus duration on behavior	33
3.3 Sensory and motor history affect behavioral choice.....	35
3.4 Whole-brain imaging uncovers neuronal correlates	40
3.5 Mapping a decision making model to the neuronal data	50
3.6 Generation of motor output.....	54
4. Discussion.....	63
4.1 The OMR as a perceptual decision task.....	63
4.2 Neural activity underlying decision making steps	65
4.3 Temporal dynamics underlying integrating activity.....	70
4.4 Concluding remarks and future directions	71
5. Appendix.....	74
5.1 Abbreviations	74
5.2 List of figures	75
References	77
List of publications.....	89
Acknowledgments	91
Eidesstattliche Versicherung/Affidavit.....	92
Declaration of author contributions.....	93

1. Introduction

1.1 Perceptual decision making

In making behavioral choices, animals combine sensory information and internal states to maximize benefits from their interaction with the external environment. As momentary sensory cues are often noisy and uncertain, in order to properly infer the state of the world, animals need to integrate sensory evidence such that it can be evaluated over longer timescales, and use this valuation to plan the appropriate motor actions. In contrast to simple reflexive behaviors, in which motor responses are immediately elicited following sensory stimuli, the process of sensory integration – the core of perceptual decisions, takes course over timescales that are orders of magnitude longer than action potentials. How such a computation is implemented at the neural level remains largely unknown.

A conceptually simple model that can describe both behavioral and neurophysiological data underlying decision processes is that of evidence accumulation (Ratcliff, 1978; Laming, 1968): in selecting a particular choice, evidence for or against different alternatives is gradually increasing, and the final value of this accumulated evidence will drive the decision outcome. The difficulty of the task is proportional with the time course of the decision process: the stronger the evidence for a particular alternative is, the faster it will reach a value that can lead to a choice selection. This ‘evidence accumulation’ model describes very well behavioral and neurophysiological results in many perceptual decision paradigms involving multiple sensory modalities, in various model organisms, including non-human primates (Newsome et al., 1989; Shadlen and Newsome, 1996; Hanes and Schall, 1996), rodents (Brunton et al., 2013; Scott, Constantinople et al., 2017; Licata et al., 2017), humans (O’Connell et al., 2012; Wyart et al., 2012), and fruit flies (Das Gupta et al., 2014; Goshner et al., 2018).

1.1.1 Neural basis of perceptual decision making

One of the most widely used paradigms in perceptual decision making studies is the random dot motion discrimination task (RDM), first used in non-human primates (Newsome and Pare, 1988; Newsome et al., 1989). In a typical experiment, subjects are trained to indicate the net direction of motion of dots moving on a screen, a fraction of which moves either to the left or the right. The difficulty of this task is varied by adjusting the coherent motion fraction. The subjects indicate their decision by making a saccade towards a target located in the corresponding motion direction (Figure 1.1a). Two variants of these tasks have been developed. In the fixed duration task (Newsome et al., 1989; Shadlen and Newsome, 1996), the subject has a limited viewing duration followed by a brief delay, after which it indicates its decision with a saccade. In the reaction time task (Roitman and Shadlen, 2002) the subject controls the viewing period duration, by performing a saccade whenever ready to commit to one of the alternatives. Behaviorally, the difficulty of the task is reflected in decision accuracy, and the reaction time, respectively (Figure 1.1b).

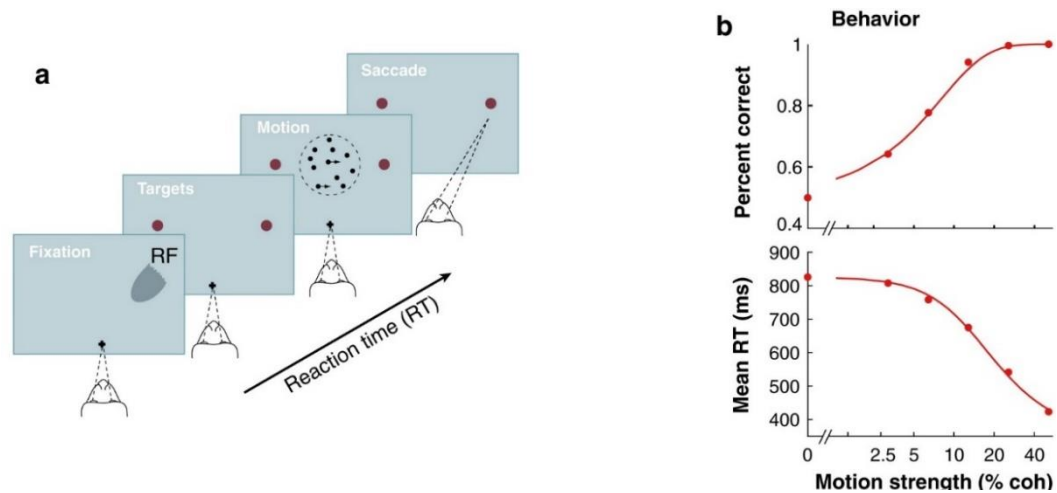


Figure 1.1 The RDM paradigm and behavioral characteristics

a. Choice-reaction time version of the task: the subject looks at a screen containing dots moving at varying coherence fractions, and decides the net direction of motion. The subject controls the viewing time and indicates the

decision by making a saccade to a peripheral target whenever ready. **b.** Effect of stimulus difficulty on accuracy and decision time. *Figure taken from Gold and Shadlen (2007), with permission.*

Seminal studies from the Newsome and Shadlen labs have first indicated a link between neural responses and evidence accumulation, based on single unit electrophysiological recordings in non-human primates. As the subjects were performing the RDM task, the firing rate of neurons in the lateral intraparietal area (LIP) of the posterior parietal cortex (PPC) was ramping up in time, in a graded manner according to the strength of the motion stimulus (Shadlen and Newsome, 1996; Shadlen and Newsome, 2001; Roitman and Shadlen, 2002) (Figure 1.2). LIP neurons were reflecting the temporal integration of noisy sensory evidence, which was encoded in the activity of direction-tuned neurons in the middle temporal area (MT) (Newsome et al., 1989, Salzman et al., 1990) (Figure 1.2, inset).

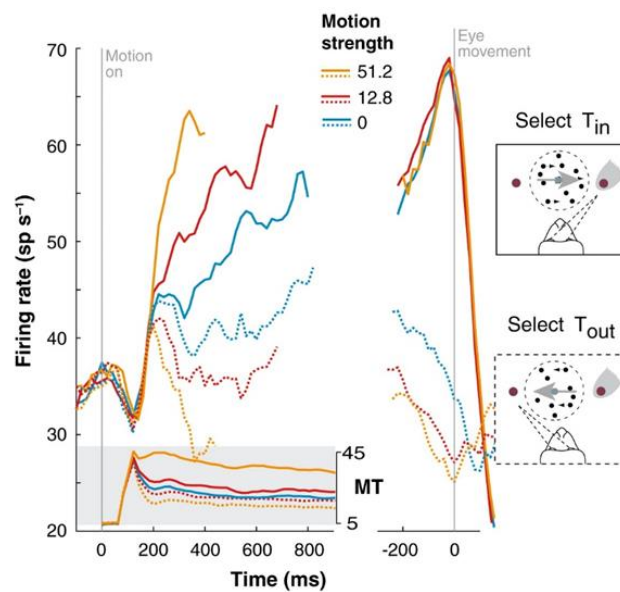


Figure 1.2 LIP firing rates approximate the integral of a difference in firing rate between MT neurons with opposite direction preferences. Average firing rate from 54 LIP neurons during the reaction time version of

the RDM task is shown for three levels of difficulty. One of the choice targets (T_{in}) is in the response field of the LIP neuron, while the other target (T_{out}) is outside of this field. Responses are grouped by motion strength and direction of choice. Left: responses are aligned to onset of random dot motion, truncated at the median reaction time or 100 ms before eye movement. Shaded insert shows average responses from direction selective neurons in area MT to motion in the preferred and non-preferred direction. Right: the responses are aligned to the eye movement. *Figure taken from Gold and Shadlen, 2007, with permission.*

Similar responses to LIP neurons have also been found in other brain regions involved with selection and preparation of eye movements, including the superior colliculus (Horwitz and Newsome, 1999, 2001; Ratcliff et al., 2003), frontal eye field (FEF) (Hanes and Schall, 1996; Gold and Shadlen, 2000, 2003; Ding and Gold, 2012; Mante et al., 2013), dorsolateral prefrontal cortex (dlPFC) (Kim and Shadlen, 1999), and the striatum (Ding and Gold, 2010) (Figure 1.3). It was not immediately obvious why the activity in all these brain regions correlated so well with the neural equivalent of an evidence accumulator, and what specific contribution each of these areas had to the decision making process. While microstimulation studies in the area MT could causally relate the activity here to the encoding of sensory evidence (Newsome et al., 1989, Salzman et al., 1990), similar perturbations in area LIP led to less conclusive results (Ditterich et al., 2003; Hanks et al.; 2006; Katz et al., 2016).

In recent studies, perceptual decision tasks have been successfully developed in rodents, facilitating experimental approaches to delineate the relevant causal circuit of evidence accumulation. In the ‘Poisson clicks’ task (Brunton et al., 2013) for example, rats are presented with randomly timed auditory pulses on both left and right side simultaneously, and are trained to orient themselves to the side that contained more clicks during a trial. The difficulty of the task here can be varied by changing the number of pulses presented on each side. This particular stimulation paradigm provided an opportunity to observe the effect of each auditory pulse in the neural activity encoding integrating

evidence. Firing rate patterns that correlate with evidence accumulation were observed in the rat PPC and the frontal orienting field (FOF) (Hanks et al., 2015), areas thought to be analogous to primate PPC and FEF, respectively (Brody and Hanks, 2016). A more careful analysis of the neural data suggested that the PPC was involved with a graded representation of the accumulator value, while the FOF turns this value into a more categorical representation (Hanks et al., 2015), implying more specific roles of these areas in the decision making process. However, similar to primate microstimulation studies in area LIP, optogenetic perturbations in rat PPC had almost no effect in the decision making performance. Brody and Hanks (2016) propose that in order to be part of the evidence accumulation circuit, a brain region should satisfy three initial criteria: (i) inactivation of the area should have a behavioral effect; (ii) perturbations during time specific windows corresponding to evidence accumulation should impact the behavior; (iii) the graded value of the accumulator should be encoded in the brain region's neural activity. In a recent study investigating the role of the striatum in the Poisson clicks task, Yartsev, Hanks et al. (2018) show that neural activity recorded here represents the graded value of accumulated evidence, inactivation of the striatum leads to deficits in task performance, and that perturbations at specific times during the accumulation process affects the decision outcome. While these results indeed conform with the suggested criteria for being part of the evidence accumulation circuit (Brody and Hanks, 2016), it remains unclear what are the specific contributions of other areas that correlate with evidence accumulation, if perhaps other brain regions not yet investigated are also involved, or the direction of information flow shaping the circuit of this computation.

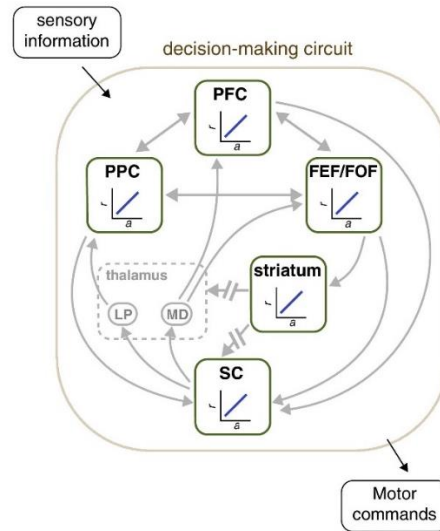


Figure 1.3 Brain regions with response profiles that correlate with accumulating evidence during decision making. PFC - prefrontal cortex; PPC - parietal cortex; FEF - frontal eye field; FOF - frontal orienting field. *Figure taken from Hanks and Brody, 2016, with permission.*

1.1.2 Theoretical models describing decision making processes

Within the framework of evidence accumulation, two main models have been proposed in terms of terminating the accumulation process and initiate the behavioral choice. In the simplest case, the ‘race model’, a decision is made as soon as the evidence supporting one alternative exceeds a threshold (Vickers, 1970). In the ‘diffusion model’, the difference between the accumulated evidence supporting one alternative as opposed to another needs to reach a threshold in order for the decision to be made (Ratcliff, 1978; Laming, 1968; Stone, 1960). As the diffusion model implements an efficient test called the sequential probability ratio test (SPRT), which optimizes decision reaction time for a required accuracy (Wald and Wolfowitz, 1948), the accumulated evidence will reach the correct decision boundary faster than the race model (Bogacz, 2007). Indeed, from several studies analyzing reaction time in various decision tasks, as well as neuronal responses, the

diffusion model could better predict behavioral data than the race model (Ratcliff and Smith, 2004; Smith and Ratcliff, 2004; Ratcliff et al., 2003).

Extensions to these evidence accumulation models have been proposed, leading to architectures that can better predict both the behavioral data as well as the neural responses underlying the process of decision making (Shadlen and Newsome, 2001; Usher and McClelland, 2001; Mazurek et al., 2003). The models involve two integrators, which accumulate evidence corresponding to each of the possible alternatives, and assume that commitment to a behavioral choice occurs when one of the integrators reaches a threshold. If the integrators solely accumulate ipsilateral sensory evidence, the model is analogous to the race model (Bogacz, 2007) (Figure 1.4, left). The integrators may additionally receive inhibitory connections, either from contralateral sensory input, as in the feedforward inhibition model (FFI) (Shadlen and Newsome, 2001; Mazurek et al., 2003), or from the opposing integrator, in the leaky competing accumulator model (LCA) (Usher and McClelland, 2001; Teodorescu and Usher, 2013) (Figure 1.4). In both of these cases, for specific parameter values adjusting the weights of the inhibition, these architectures can be effectively reduced to the diffusion model. Different architectures of the diffusion model can lead to slightly different predictions regarding the firing rate of the integrators. For example, in the FFI model, the integrator firing rate depends only on the difference between the two sensory inputs, while in the LCA model, the firing rate will be dependent on the total sensory input. By carefully analyzing which of the models better fits the neurophysiological data, specific predictions can be made about the functional connectivity of the integrating circuit underlying the decision making process.

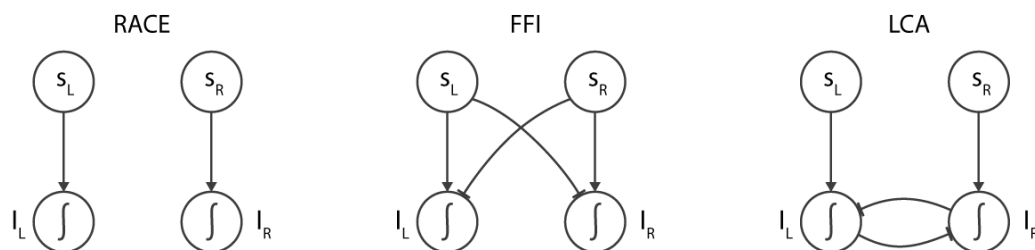


Figure 1.4 Proposed decision making model architectures. Left: the race model, comprising of two integrators that independently accumulate

evidence. Middle: the FFI model, where the two integrators receive inhibitory connections from the sensory input. Right: the LCA model, where the integrators receive contralateral inhibition coming from the opposing integrator.

1.2 The larval zebrafish as a model organism in systems neuroscience

The larval zebrafish (*Danio rerio*) has recently emerged as a powerful model organism in the study of systems neuroscience. Its small size, translucent brain, and rich genetic and molecular tools, have made it particularly appealing for the investigation of neural circuits underlying behavior. Zebrafish exhibit a rich behavioral repertoire, ranging from innate reflexive behaviors such as the optomotor response (OMR) (Orger et al, 2008), the optokinetic response (OKR) (Easter and Nicola, 1997), phototaxis (Wolf et al., 2017), to more complex behaviors such as prey capture (Bianco et al., 2011), learned motor adaptation (Portugues and Engert, 2011, Ahrens et al., 2012) and associative learning (Aizenberg and Schuman, 2011). Given the powerful optical methods available for recording and manipulating brain activity (Kerr and Denk, 2008; Ahrens et al., 2013; Panier et al., 2013; Portugues et al., 2013), significant advances have been made in deciphering the sensorimotor processing and functional circuits underlying these behaviors.

1.2.1 Zebrafish neuroanatomy

The larval zebrafish brain contains about 100,000 neurons (Naumann et al., 2010), distributed into 3 main regions: the forebrain, midbrain and hindbrain (Figure 1.3). The forebrain (comprising of the telencephalon and diencephalon) contains nuclei analogous to the mammalian basal ganglia, amygdala, hippocampus, habenula and thalamus, among other structures (Mueller and Wullimann, 2016). Several studies have implicated these

brain areas in complex cognitive functions, involving motivation, emotion and memory related processes (Aoki et al., 2013; Amo et al., 2014; Cheng et al., 2014; Chen et al., 2019). Dorsally located in the midbrain is the optic tectum, homolog of the mammalian superior colliculus, and immediately ventral, the pretectum, analogous to the nucleus of the optic tract (NOT). Both structures are directly involved with visual processing and have been implicated in a variety of visually mediated behaviors (Gahtan et al., 2005; Kubo et al., 2014; Portugues, Feierstein et al., 2014; Naumann et al., 2016). The hindbrain, containing the cerebellum, reticular formation, dorsal and medial raphe nuclei, and clusters of reticulospinal premotor neurons, is mostly involved in modulating motor activity (Orger et al., 2008; Severi, Portugues et al., 2014; Dunn et al., 2016; Kawashima et al., 2016; Knogler et al., 2019).

Many transgenic lines are available, generated either by random enhancer trapping (Scott et al., 2007) or by labeling populations expressing particular genetic markers (Suster et al., 2009), allowing for the expression of specific genes in genetically defined neuronal populations. For example, Figure 1.5 shows the distribution of particular neurotransmitter classes throughout the entire brain of a 6 days post fertilization (dpf) zebrafish, highlighting the dorsal raphe serotonergic neurons (DRN), or various dopaminergic clusters, including the caudal and ventral hypothalamus or the posterior tuberculum in the midbrain.

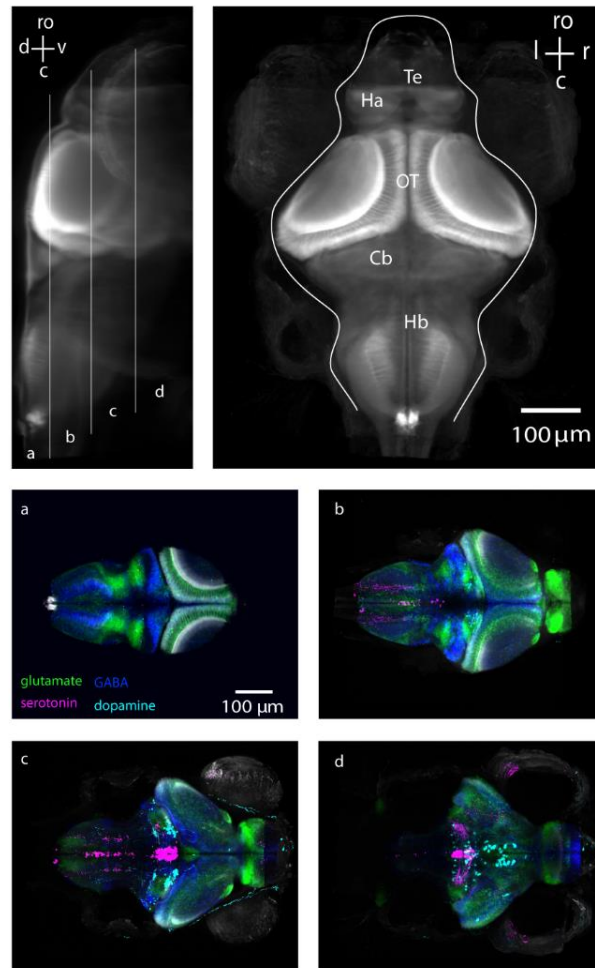


Figure 1.5 Brain of a 6 dpf zebrafish. Top: Lateral and dorsoventral projections of an *elavl3:GCaMP6f* zebrafish larva. Bottom: Dorsoventral projections of sections labeled in the lateral view in the top panel, marking glutamatergic, GABAergic, serotonergic and dopaminergic neuronal populations (markers are expressed under the *vglut2*, *gad1b*, *tph2* and *th* promoters). Te: telencephalon; Ha: habenula; OT: optic tectum; Cb: cerebellum; Hb: hindbrain.

1.2.2 Optical tools for dissecting behavioral neural circuits

The transparency of the zebrafish larva offers unparalleled advantages for functional imaging: combining two-photon microscopy (Denk et al., 1990) with expression of genetically encoded calcium indicators enables visualization of whole brain activity at single cell resolution in the intact, behaving animal. This technique has been successfully used in a number of studies probing different behaviors, such as the OKR (Portugues, Feierstein et al., 2014), motor adaptation (Ahrens et al., 2012), phototaxis (Wolf et al., 2017) or the OMR (Naumann et al., 2016). As these studies have shown, the neural activity underlying these behaviors is distributed in several clusters throughout the brain (Figure 1.6), highlighting the great advantage of having access to the whole brain activity. Additionally, optical control of specific neuronal populations can be achieved remotely in a completely non-invasive manner, by targeted expression of light-gated ion channels such as channelrhodopsin or halorhodopsin (Portugues et al., 2013). Studies using optogenetic loss- and gain-of-function manipulations have been successful in identifying a hindbrain area involved in saccadic eye movements (Schoonheim et al., 2010), a role for the DRN in mediating motor learning (Kawashima et al., 2016), eliciting an escape response by inducing single spikes in sensory neurons (Douglass et al., 2008), among others. Targeted ablations of specific neurons or populations using high power lasers have also contributed to establishing causality of particular brain areas to specific behaviors - for example, a subset of hindbrain neurons involved in an escape response (Liu and Fetcho, 1999), or selective impairment of prey capture behavior following retinotectal ablations (Roeser and Baier, 2003; Gahtan et al, 2005). The effect of these manipulations can then be simultaneously investigated at the level of behavior and its underlying neural activity or functional circuit.

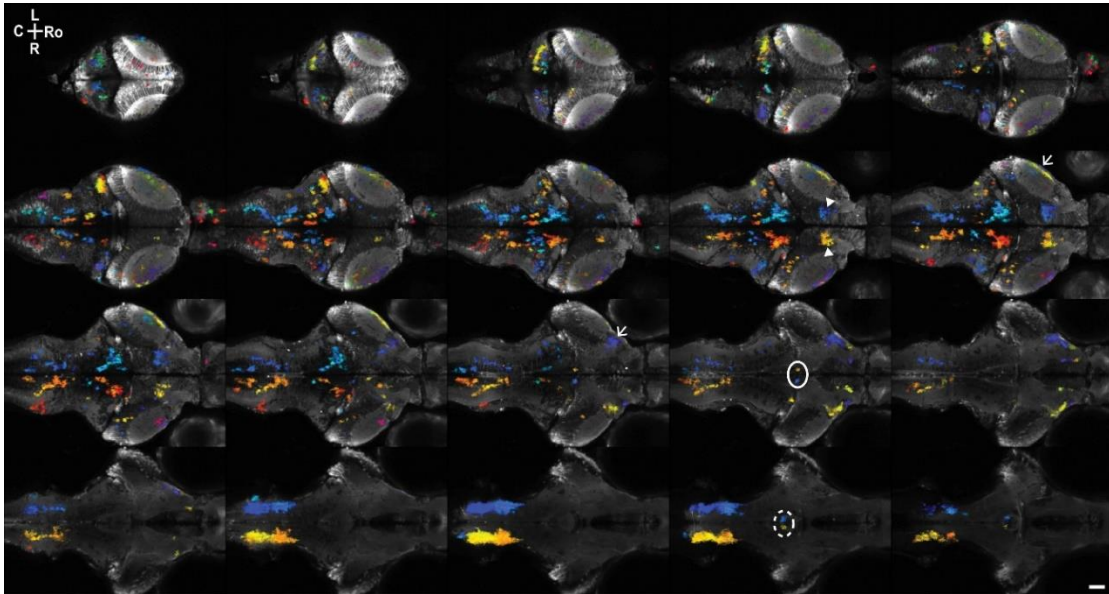


Figure 1.6 Comprehensive map of brain areas that are active during the OKR behavior. ROIs are color-coded depending on the specific phase within a periodic sensory stimulus at which they are activated. Features highlighted are the oculomotor nucleus (solid line), the interpeduncular nucleus/median raphe (dashed line), the pretectum (arrowheads), and retinal ganglion cell arborization fields (arrows). *Figure taken from Portugues, Feierstein et al. (2014), with permission.*

1.2.3 The zebrafish optomotor response

In the optomotor response (OMR), fish use whole-field visual motion cues to align themselves and swim in the direction of perceived motion, ensuring they maintain a stable position in relation to their environment (Portugues and Engert, 2009). This behavior has an important ethological function, helping fish maintain their location in a water flow, and preventing them from being carried downstream. Zebrafish larvae begin responding to moving stimuli shortly after hatching, and by 6-7 dpf, the OMR can be reliably evoked

(Neuhauss et al., 1996). In the laboratory setup, the OMR can be elicited by displaying whole-field moving gratings from below (Orger et al., 2000, 2008), even as the larva is head-restrained agarose, with only the tail free to move (Portugues and Engert, 2011). Fish swim in discrete bouts, comprised of multiple tail oscillations, which are separated by brief periods of inactivity (Budick and O'Malley, 2000), and specific locomotor parameters such as bout duration, or inter-bout interval are modulated depending on the strength of the visual motion (controlled in turn by parameters such as speed, spatial and temporal frequency of the gratings presented) (Severi, Portugues et al., 2014; Maaswinkel and Li, 2003). As opposed to other visually driven reflexive behaviors, the OMR exhibits a relatively long latency to swim initiation, and this latency is further modulated by the speed of the visual motion stimulus (Portugues et al., 2015).

In terms of underlying neural activity, bilateral tectal ablation did not abolish the OMR (Roeser and Baier, 2003), implying a non-tectal visual processing path in controlling this behavior. Several studies focused on the role of reticulospinal neurons in the OMR, especially in the nucleus of the medial longitudinal fasciculus (nMLF), showing that distinct clusters correlate with various locomotor kinematics, including speed and duration of swim bouts (Orger et al., 2008; Huang et al., 2013; Thiele et al., 2014; Severi et al., 2014). Finally, using a whole brain imaging approach, Naumann et al. (2016) show that diverse neural responses underlying the OMR are distributed across the brain, from integration of binocular and direction-specific visual streams in the pretectum, to signals acutely related to directional turning and forward swims in the anterior hindbrain, nMLF and ventromedial spinal neurons.

1.3 Thesis objectives

This study aims to investigate the neural correlates underlying a perceptual decision making task. Previous studies identified neural activity related to decision-making mechanisms in a number of brain regions, however, their explicit contributions to this process is controversial and the precise flow of information throughout these regions remains unclear (Katz et al., 2016; Hanks et al., 2005; Brody and Hanks, 2016). One of the main limitations comes from the restricted access to the brain areas involved: most neurophysiological insights are from single unit recordings or calcium imaging over a limited field of view. In this study, I attempted to circumvent some of these limitations by developing a perceptual decision-making assay in the larval zebrafish, and using its unique features that enable brain wide interrogation of neural activity during behavior.

I first adapted the classic RDM paradigm to the zebrafish, using the left/right OMR as a decision readout. In the typical RDM paradigms, animals are first trained using reward reinforcement during the acquisition phase to perform the task. When performance stops improving, testing occurs: this latter phase allows the study of perceptual decision making irrespective of reward. In the assay presented here, zebrafish larvae use noisy sensory cues to estimate the state of their visual environment and update this estimate with the continuous inflow of sensory evidence. This assay does not involve operant conditioning, therefore the neuronal correlates of pure perceptual decision making can be isolated, independently from reward related activity. I show that fish modulate their turning behavior depending on the visual motion strength as well as the sensory and motor history, in a similar way to how these parameters affect decision making in the primate RDM tasks, thus validating this assay for investigation of neural correlates of decision making circuits.

After adapting this assay in a head restrained paradigm, I used cellular resolution whole-brain imaging in intact, behaving animals to identify all neural signals relevant to the different stages of the decision-making process, from momentary sensory evaluation, accumulation of this sensory evidence and behavioral output. These neural correlates are localized in several anatomical clusters distributed across the brain, and are lateralized based on stimulus direction. Within the framework of a generalized sensory integrator model, the identified neural responses representing accumulating sensory evidence exhibit

a continuous distribution of time constants, with different units integrating evidence over varying time windows, reminiscent of neural activity representing sensory history found in other decision-making studies (Akrami et al., 2018; Scott, Constantinople et al., 2017). These identified integrating units are also distributed across different regions, suggesting that decision-making activity is represented broadly across the brain.

In order to link this integrated sensory evidence with the behavioral output, a turning rate model was established, based on a probabilistic readout of the sensory evidence variable, which is derived from bidirectional integration. An unbiased whole-brain analysis reveals that the majority of turning rate encoding units are located in the interpeduncular nucleus (IPN), a circular structure in the ventral midbrain-hindbrain boundary, which has been previously shown to correlate with locomotor and navigation related variables (Sharp et al., 2006; Clark and Taube, 2009).

2. Materials and Methods

2.1 Zebrafish husbandry

All experiments were performed with 6-7 days post fertilization (dpf) zebrafish larvae (*Danio rerio*). The Tuepfel long-fin (TL) wild type strain was used for freely swimming behavioral experiments. The nacre (*mitfa*^{-/-}) transgenic zebrafish lines Tg(*elavl3:GCaMP6s*^{+/+}) (Kim et al., 2017) and Tg(*elavl3:GCaMP6f*^{+/+}) (Wolf et al., 2017) were used for functional imaging experiments. Zebrafish larvae were obtained by mating three adult pairs in one mating tank simultaneously. Larvae were kept in 8.8 cm Petri dishes (about 25 larvae per dish) half filled with Danieau buffer (17 mM NaCl, 2 mM KCl, 0.12 mM MgSO₂, 1.8 mM Ca(NO₃)₂, 1.5 mM HEPES) for the first day of development, and water from the fish facility starting from the second day. Fish and larvae were maintained at 28 degrees on a 14h-10h light-dark cycle. All animal experimental procedures were approved by the Max Planck Society and the local government (Regierung von Oberbayern).

2.2 Freely-swimming behavioral experiments

2.2.1 Behavioral Setup

Larval zebrafish were placed in an 8.8 cm Petri dish half filled with fish water, on top of a diffusive screen mounted on a clear acrylic support, and illuminated from below using an array of IR LEDs (Fig 1). Freely swimming larvae were monitored using a high speed camera (Mikrotron) running at 200 fps, equipped with a lens (Edmund Optics) and

a IR band pass filter. The visual stimuli were displayed from below using an Asus P2E microprojector and a cold mirror (Edmund Optics).

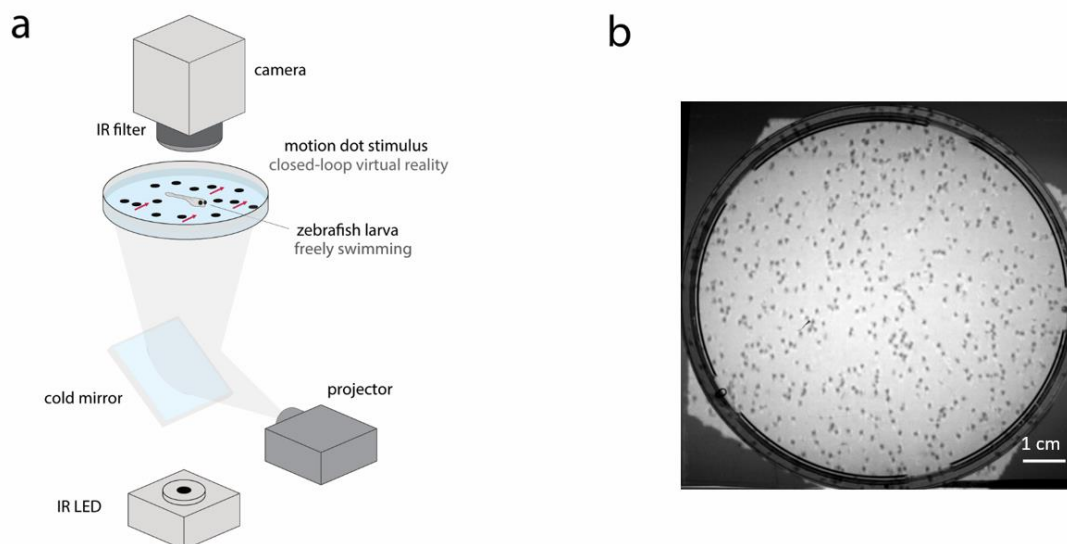


Figure 2.1 Freely swimming behavioral setup

a. Schematic of the behavioral closed-loop setup used for freely swimming experiments. **b.** Freely swimming fish with the random dot motion stimulus projected from below. *Figure adapted from Dragomir et al. (under review)*

2.2.2 Visual motion stimulus

The stimulus consisted of randomly moving dots, a fraction of which moved coherently to the left or to the right of the fish (Figure 2.2). The stimulus was constructed such that dots had a limited lifetime of 50 ms, to prevent fish from following individual dots. Custom written software in LabView was used for tracking of the fish swim dynamics and for generating the closed loop random dot motion stimulus. Fish orientation was

constantly monitored and after each turn, the direction of the coherent dot motion was immediately updated, such that its direction remained constant with respect to the axis of the fish. If the fish approached the edges of the dish (less than 1 cm away, as shown in Figure 2.3), the coherence stimulus was interrupted and replaced with a concentric inward moving circular grating stimulus, meant to bring the fish back into the center of the dish and thus avoid wall following behavior (thigmotaxis). The coherence stimulus that was shown previously was restarted as soon as the fish was in the inner part of the dish again. Only complete trials of coherence stimulus (uninterrupted by moving concentric circles) were further used for behavioral analysis.

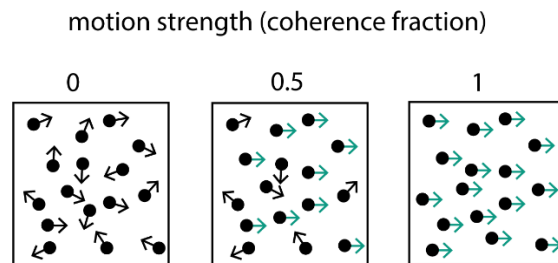


Figure 2.2 Schematic of visual motion stimulus, displaying 3 different examples of motion strengths: 0, 0.5 and 1 coherence. *Figure adapted from Dragomir et al. (under review)*

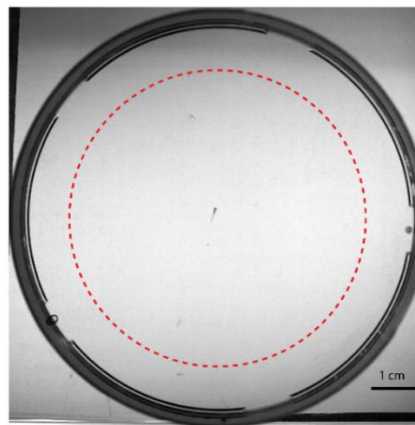


Figure 2.3 Freely swimming area is restricted to the inner part of the dish (delineated by the red dotted line, invisible to the fish)

2.2.3 Stimulus protocol

Three different protocols were used in the freely swimming behavior experiments. In the randomized coherence experiments, the coherence fraction ranged from -1 (left) to +1 (right), in increments of 0.1, and was maintained constant for the 12 second time interval that constitutes a trial, before being immediately changed to a new value in a next trial. A set of stimuli consisted of 22 trials, containing coherences of all magnitudes in both directions, and presented in a randomized order. In a given experiment, fish had to complete at least five sets of stimuli.

In the varying pulse duration experiments, trials contained only coherences of magnitude 0.3, 0.6 and 1, in both directions. Trials were presented as pulses of 1, 2, 3, 4, 6, 8 and 10 s coherence motion, preceded and followed by 6 s of coherence 0. The sequence of coherence magnitudes and direction was randomized, and one experiment contained all possible combinations of stimulus magnitude, direction and spurt duration.

In the fixed transition experiments, trials contained only coherences of magnitude 0.3, 0.6 and 1, in both directions, immediately following one another. A set of stimuli contained all possible combinations of transition involving coherence magnitude and coherence direction, and all possible transitions were probed an equal number of times. In a given experiment, fish had to complete at least five sets of stimuli in order to be included into the dataset.

2.2.4 Behavioral tracking

For generating the closed loop stimulation, fish position and orientation was computed in real time with custom written software in LabView. Fish position was detected using background subtraction, which was calculated as an average of the frames captured in the first 10 s of the experiment. To eliminate point pixel noise, a morphological open operation was applied, and the fish was detected as the particle with the largest area in the frame. The orientation of the fish was expressed as the angular coordinate of the heading vector in relation to a polar coordinate system. The end point of the heading vector was

identified as the darkest pixel in the fish (the head), while the initial point of the vector was calculated as the darkest pixel in a circle around the head (which corresponded with the tail of the fish).

Further behavioral analysis was carried out with custom written software in MATLAB. For swim bout detection, the displacement in the fish position coordinates was calculated and then filtered with a low pass filter to eliminate high frequency noise. The distance moved was then computed as the square root of the sum of the displacements squared. A bout was identified by peak finding in the swimming velocity trace obtained from the smoothed frame by frame position of the fish. Bouts during which displacement was smaller than 1 mm were considered noise. This was checked by looking at the video.

2.3 Head-restrained behavioral experiments

2.3.1 Behavioral setup

Larvae were placed individually in 3.5 cm Petri dishes and embedded in 1.5 % low melting agarose. The agarose around the tail, caudal to the pectoral fins was cut away with a fine scalpel to allow for tail movement. The fish were then placed on top of a diffusive screen mounted on a clear acrylic support, and illuminated from below using an IR LED. Embedded larvae were monitored using a high speed camera (Pike F032B, Allied Vision Technologies) running at 200 fps, equipped with a lens (Edmund Optics) and an IR band pass filter. The visual stimuli were displayed from below using an Asus P2E microprojector and a cold mirror (Edmund Optics).

2.3.2 Visual motion stimulus

The visual motion stimulus (as described above in Methods section 2.2.2) was implemented in an open loop fashion with custom written software in Python.

2.3.3 Stimulus protocol

For the head embedded behavioral experiments, a full experiment consisted of 30 trial sets. Each set consisted of 7 trials, probing coherence magnitudes of 0, 0.3, 0.6 and 1 in both directions, and presented in a randomized order. Each coherence was presented during a 20 s trial, and was preceded and followed by a 5 s pause of no motion (with dots remaining on the screen).

2.3.4 Behavioral tracking and bout categorization

Custom written software in Python was used for tracking tail movement of the fish. The start and end position of the tail was first manually indicated for each fish. Following tail segmentation based on centers of mass of sampling windows (Stih, Petrucco et al., 2019), the total curvature was calculated as the difference in angle between the first and last tail segment.

Further behavioral analysis was done with custom written software in MATLAB. For each bout, a laterality index was computed by adding the cumulative tail angle recorded for the first 60 ms of the bout (Figure 3.8a), as this is the time frame over which forward swims and turns differ most prominently (Huang et al., 2013). For every fish, the histogram of laterality indices across all bouts in all conditions was plotted and fit with the sum of three Gaussian distributions (Figure 3.8b). This ensures that differences in the embedding and preparation are accounted for in a fish by fish basis. The two minima between the three peaks were chosen as the thresholds to distinguish between the three types of swim bout: forward and left and right turns.

2.4 Whole-brain imaging experiments

2.4.1 Two-Photon Calcium Imaging setup and acquisition

Larvae were placed in 3.5 cm Petri dishes and embedded in 1.5-2% agarose prior to imaging. The agarose around the tail, caudal to the pectoral fins was cut away with a fine scalpel to allow for tail movement. The dish was placed onto an acrylic support with a light-diffusing screen and imaged on a custom-built two-photon microscope. A Ti:Sapphire laser (Spectra Physics Mai Tai) tuned to 905 nm was used for excitation. Larval brains were imaged while being presented the random dot motion visual stimuli. Visual stimuli (see above in Methods section 2.2.2) were generated using a custom written Python script, and were projected at 60 frames per second using an Asus P2E microprojector and a red long-pass filter (Kodak Wratten No.25) to allow for simultaneous imaging and visual stimulation. Full frames were acquired every 334.51 ms in four, 0.83- μ m-spaced interlaced scans, which resulted in x and y pixel dimension between 0.51 and 1 μ m (varying resolutions depended on field of view covered). Imaging stacks were mostly acquired in the dorsal to ventral direction, and for some fish (covering deep hindbrain areas) in the ventral to dorsal direction. In order to track the behavior, fish were illuminated from above using an infrared LED (850 nm wavelength) and the fish was imaged from below at 200 frames per second using an infrared-sensitive charge-coupled device camera (Pike F032B, Allied Vision Technologies). Tail movement was monitored using custom written software in Python.

2.4.2 Stimulus protocol

Two types of experimental paradigms were used: one in which the stimulus sequence was randomized and coherences were separated by pauses of no dot motion, and

another in which coherences directly followed one another, with no pauses, in a nonrandomized fashion. In the randomized paradigm, the set of stimuli used in imaging experiments consisted of coherences 0, 0.3, 0.6, and 1, in both directions, with a duration of 30 s, and separated by 10 s of pause (dots remained on the screen but were static). In the direct transition paradigm, coherences 0.8, 0.3 and 0 were probed, with no break in between, and sampling every possible transition between direction and coherence magnitude. After all stimuli were shown in one plane, the focal plane was shifted ventrally or dorsally by 2 μm (for some fish 1 μm) and the process was repeated, with either the randomized sequence or direct transition of stimuli in each plane.

2.4.3 Image analysis

Image analysis was performed with custom written scripts in MATLAB, as previously described in Portugues, Feierstein et al. (2014). To correct for motion during imaging, the imaged frames were first aligned to the average image of the corresponding plane, followed by alignment across all z-planes. Automated algorithms were used for ROI segmentation, based on local pixel correlations. First, a three dimensional anatomical stack of correlation values was obtained by finding voxels whose activity correlates closely with that of neighboring ones. ROI segmentation begins with selecting the voxel with the highest local correlation value (the seed of the ROI). Then, all the neighboring voxels whose activity correlation with the seed voxel exceeds a threshold value of 0.5 are added to the ROI. The process is then repeated with the neighboring voxels of the newly expanded ROI. To ensure there are no holes within the ROIs, a morphological close operation was applied, incorporating any voxels that were not yet included in the ROI, but whose neighboring voxels were. If no more voxels are added, the current ROI segmentation is complete, and a new seed is picked for the next ROI to be segmented (the next highest correlation value in the anatomical correlation stack). To minimize the possibility of constructing ROIs from noise, ROIs smaller than 50 voxels were discarded. When ROIs reached a size of 300 voxels (the approximate size of a neuron cell body) the process was stopped and segmentation of a new ROI began.

The fluorescence activity trace for the ROI was the sum of the fluorescence of the individual pixels belonging to the ROI. The activity was normalized by z-scoring (subtracting the mean and dividing by the standard deviation).

2.4.4 Anatomical registration

Image registration for two-photon imaging was performed using the free Computational Morphometry Toolkit (CMTK; <http://www.nitrc.org/projects/cmtk/>) (Rohlfing and Maurer, 2003), as previously described in Portugues, Feierstein et al. (2014). Anatomical stacks were made by summing the fluorescence in all the planes. The affine function was used to align each fish's anatomical stack to a lab reference brain. The transformation computed following this alignment were then used to morph individual ROIs from each fish into the reference brain.

2.4.5 Regressors and correlation analysis

Regressors for correlation analysis (as described in Portugues, Feierstein et al., 2014) were constructed from a set of sensory stimulus and motor related variables, such as presence of motion stimulus, integration of motion stimulus (uni- and bi-directional), acute motor responses (forward swims and lateralized turns), among others (full list is displayed in Figure 3.11). These were convolved with a kernel with an exponential decay based on the measured half-decay time for GCaMP6s (1.796 s) and GCaMP6f (0.4 s) (Chen et al., 2013) to produce a set of predicted fluorescence traces, and were correlated with the measured fluorescence traces. Correlation analysis was performed for automatically segmented ROIs to identify the variable that best described the signal of individual neurons. To assign voxels to a particular functional group, a threshold of at least 0.5 for the best absolute correlation coefficient was required (except for the all motion and unilateral integration regressors, which had a correlation threshold value of 0.3), as indicated from previous studies and shuffled controls not shown.

2.4.6 Computation of motor triggers

Motor related analysis during the imaging experiments was performed as described above (Methods section 2.3.4). In addition, the fluorescence of ROIs triggered on motor events, referred to as motor triggers, was also computed. A set of interesting features of neuronal activity that could be associated with motor activity was defined. This set comprised of the triggers shown in Figure 3.20, including the additive inverse of the trigger in 3.20d. The motor event can be a leftward turn, a rightward turn or a forward swim. All ROIs with a correlation value with the motor trigger greater than 0.7 were included.

2.5 Model fitting

2.5.1 Logistic multivariate regression model

In order to identify the dependence of the turning behavior on the current stimulus, the stimuli being presented during previous bouts and the motor output of the previous bouts, a logistic multivariate regression model was implemented. This expresses the likelihood odds ratio as a sum:

$$\log \left(\frac{P_L}{P_R} \right) = K + \sum_{i=0}^k \alpha_i C_i + \sum_{i=1}^k \beta_i B_i$$

where C_i labels the stimulus being presented, B_i the motor output of the previous i -th bout, K represents the bias and up to the k -th previous bout is considered. Rightwards bouts were set to belong to category 2, leftwards bouts to belong to category 1, rightwards coherences were set as negative, and leftwards ones positive. A dataset comprising 126754 total bouts across 5688 trials (lasting 30 seconds each) was collected across 37 fish and the model was fit using the `mrnfit` function in Matlab for each fish and then averaged across fish.

Significant coefficients were determined by testing whether the distribution of the particular coefficient (across fish) was significantly different from zero. The results are shown in Figure 3.7.

2.5.2 Generalized integrator model

(contribution of Vilim Štih)

To explain the stimulus-related responses a model based on the feedforward inhibition integrator (FFI) (Shadlen and Newsome, 2001) was constructed. As responses were frequently observed with different time constants for ipsi and contralateral excitation, independent integration of motion to both sides was allowed for, and a weighted sum was computed. The model is depicted in Figure 3.14a and is described by the following equations:

$$\begin{aligned}\tau_L \frac{dI_L}{dt} &= Ls_L^P - I_L \\ \tau_R \frac{dI_R}{dt} &= Rs_R^P - I_R \\ a &= I_L + I_R\end{aligned}$$

where I_L and I_R are the levels of integrators, τ_L and τ_R their respective time constants, L and R the input stimulus weights, S_L and S_R the current coherences to the left and right side, P the power of the nonlinearity and a the level of activity of the modeled unit.

Within the parameter space of this model are responses which are driven purely by momentary evidence, and no integration takes place (both τ_L and τ_R are around 0), responses which can be explained as a single integrator (τ_L and τ_R are equal) and responses to a single motion direction (either R or L weights are 0). The model allows for a nonlinear response to motion coherence, however by regularized fitting almost no units where this nonlinearity is present were found. This model was fitted to all ROIs spanning more than one plane and retained those whose unexplained variance was smaller than 0.4 of the variance of the trace. The model was implemented as a function in the Julia language, with

exact integration (as the system is linear after the input nonlinearity) and application of an exponential kernel with the GCaMP6s time constant. The model fit was optimized using the gradient-based BFGS method, as implemented in the Optim.jl Julia package (Mogensen et al., 2018). 3-fold cross validation was used to determine the regularization parameter λ which weighted a sum of the absolute values of the model features (weights, time constants, difference of time constants and the logarithm of the power of the nonlinearity). Significance was determined by leave-one-out cross-validation.

2.5.3 Poisson model for generation of turns

(contribution of Vilim Štíh)

The proposed integrator model architecture can be extended to explain the turning behavior: the output of two symmetrically built modules (as in Figure 3.14a) modulates linearly the deviation from the baseline rate of a Poisson process that initiates turns. All the parameters for this model were determined from behavioral experiments: first, the data of turn rates for each coherence (Figure 3.3a) was used to determine the steady-state parameters and the baseline rate of turns. This fixes the nonlinearity power P and the relative weights of inputs to the integrators in the contra or ipsilateral side. Then, from the transition experiments in Figure 3.5, the three remaining free parameters were determined: the angle of a turn, and the time constants τ_I (for ipsilateral input) and τ_C (for contralateral input). Equally good fits can be obtained for different choices of τ_I and τ_C , so the point in parameter space where they are equal was decided for. This results in a simpler model of turn generation, where instead of two Figure 3.14a modules there is only one, with additional inhibitory connection to the contralateral integrator, and where both of the integrators have the same time constant and directly modify the Poisson rate for the respective side.

2.5.4 Generation of synthetic freely-swimming behavior

In the freely swimming experiments, all stimulus coherences from -1 to +1 in 0.1 steps were tested with random transitions. In order to generate the traces shown in Figure 3.17-iii the transitions which appear in the stimulus sequence shown in Figure 3.17-i were identified, and 10 s of the pre-transition behavior and 10 s of the post-transition behavior were selected. This allowed for constructing an estimate of the expected behavior to this stimulus sequence for every fish tested.

3. Results

3.1 The optomotor response as a function of coherence

In order to investigate whether larval zebrafish modulate their behavior when exposed to visual motion of varying strength, freely swimming larval zebrafish were presented with a coherent dot motion stimulus projected from below. The coherence of the stimulus was controlled such that a fraction of dots, ranging from 0 to 1, moved either to the left or the right of the fish, with the remaining fraction moving randomly (see Methods section 2.2.2 for details). The fish were tracked in real time and a closed-loop assay (Orger et al., 2008) was implemented such that the direction of the stimulus relative to the fish's orientation remained constant in time throughout a twelve-second trial despite the fish turning (Methods section 2.2.1 and Figure 2.1).

Turning behavior was quantified by plotting the cumulative angle turned during individual trials, and then averaging for all coherences across all fish probed (Figure 3.1). Over a twelve-second trial, the total angle turned by larvae depended on the stimulus coherence, and was larger in magnitude with increasing coherence (Figure 3.1b). All swimming bouts were next divided into left turns, right turns and forward swims: plotting the distance moved and angle turned in each bout (Figure 3.2) indicated a separation between lateralized turns (which usually occurred around 25 degrees) and forward swims (centered around 0 degrees). While the number of forward swims did not change across different coherences, there were more left and right turns for higher coherences in the left- and right-ward direction, respectively (Figure 3.3a). Defining a correct turn to be one in the direction of the effective stimulus direction, the fraction of correct turns increased from 0.5 for no coherence to 0.8 for a fully coherent stimulus (Figure 3.3b, top). In addition, the latency to the first correct turn from stimulus onset became shorter as the coherence fraction increased, from over 4 seconds at low coherences to just over 3 seconds for high ones

(Figure 3.3b, bottom). Improved turning accuracy was also apparent as the time and bout number progressed within the trial (Figure 3.3c), suggesting fish are accumulating evidence to enhance their behavior.

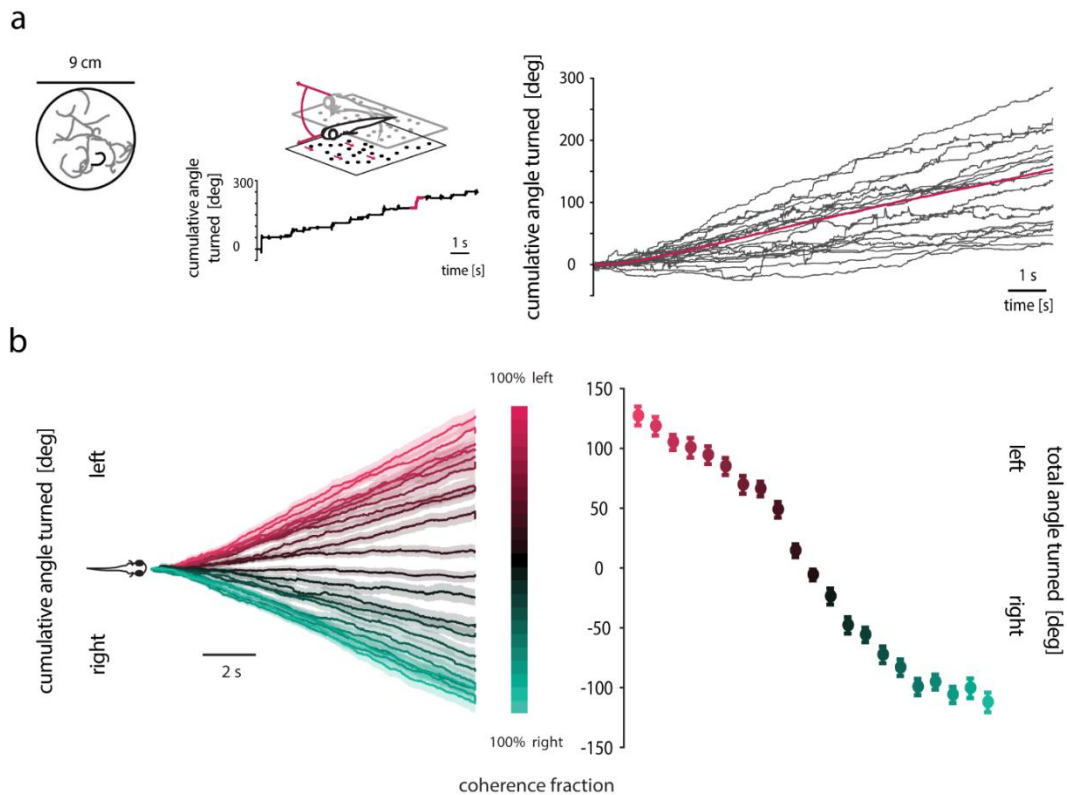


Figure 3.1 Turning behavior in freely swimming experiments

a. Left: swimming trajectories from all trials of leftwards 0.6 coherence during a freely swimming experiment shown in the dish; the highlighted trajectory is recorded during one trial and its cumulative angle turned is displayed. Right: Cumulative angle turned for all the trajectories shown in the dish on the left (for leftwards 0.6 coherence). The red line represents the average cumulative angle turned for this coherence in one fish. **b.** Left: average cumulative angle turned across all fish, for all coherences (N=55 fish, comprising of a total of 11733 trials, 95981 bouts). Right: average of total angle turned across all fish during all trial coherences. Bars and shaded

intervals represent SEM. *Figure adapted from Dragomir et al. (under review)*

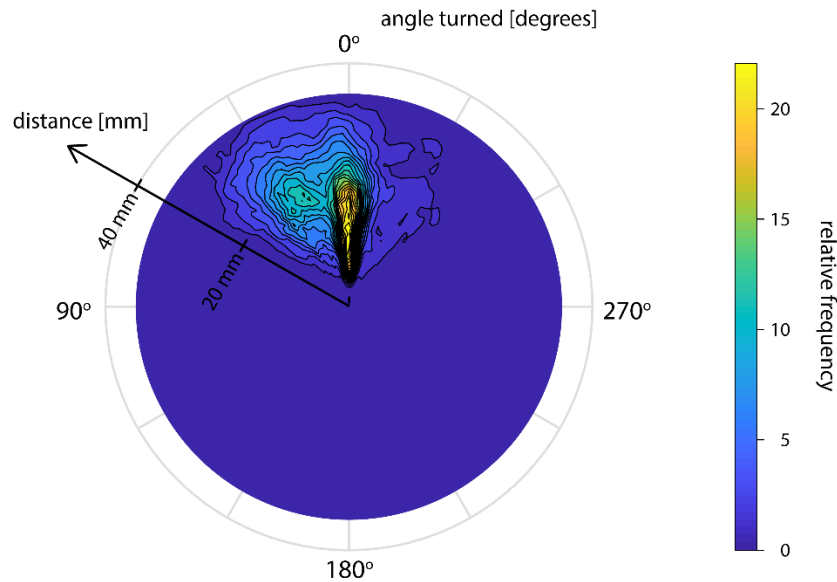


Figure 3.2 Categorization of a turn

Two-dimensional contour plot showing the distance moved and angle turned averaged across all fish when presented with coherence > 0.5 . Most swim bout events are clustered around 0 degrees, and represent forward swims, while lateralized turns begin after 15 degrees. *Figure taken from Dragomir et al. (under review)*

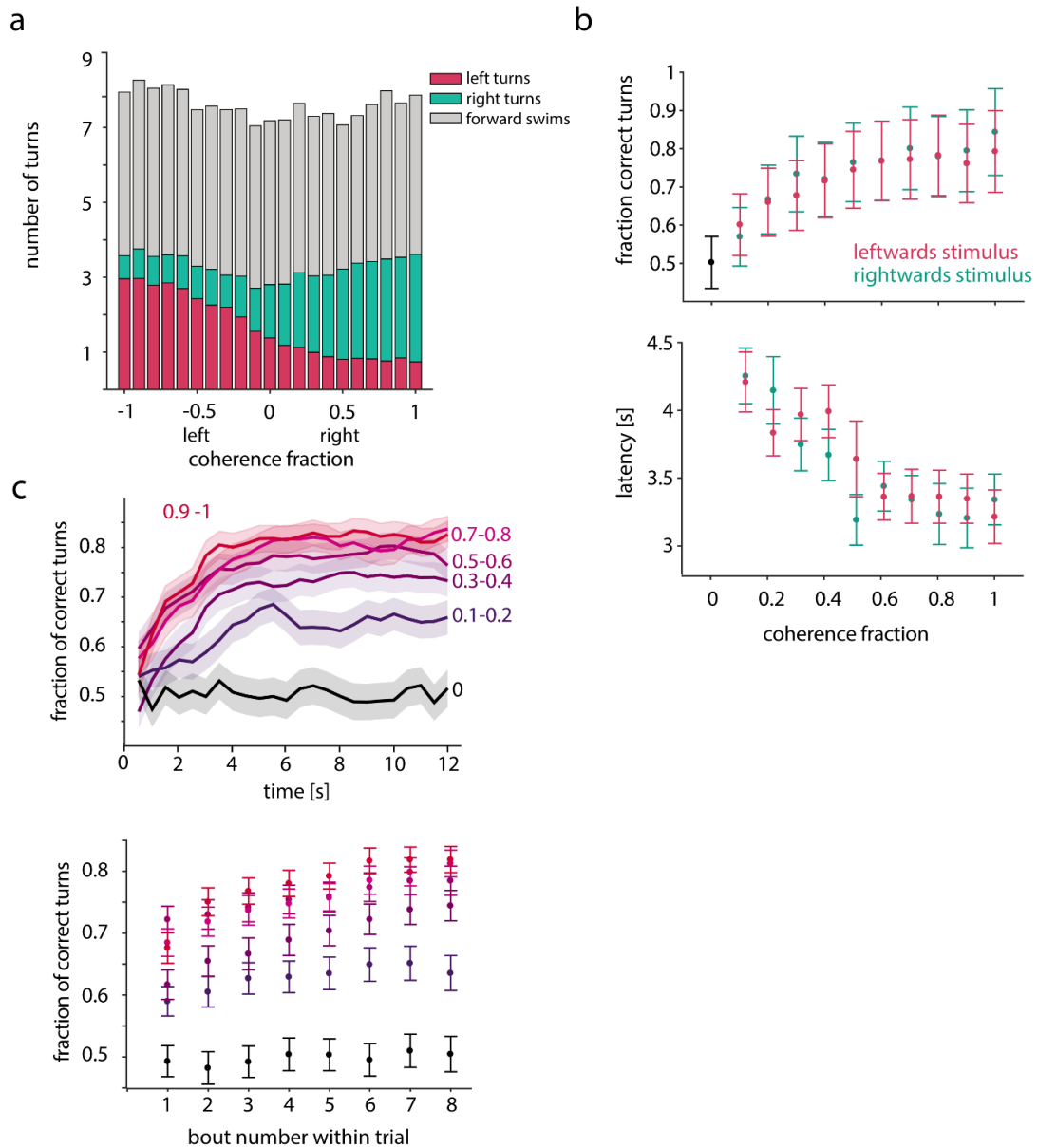


Figure 3.3 Coherence-dependent turning behavior in freely swimming experiments

a. Number of left, right and forward swims as a function of stimulus coherence. **b.** Top: Fraction of correct turns (in the direction of presented coherence). Bottom: Latency (time from stimulus onset) to first correct turn as a fraction of stimulus coherence. **c.** Fraction of correct turns as a function

of time (top) and trial bout number (bottom), for different coherence categories, averaged across all fish (N=55 fish, 11733 trials, 95981 bouts). All error bars and shaded intervals denote SEM. *Figure adapted from Dragomir et al. (under review)*

3.2 Effect of motion stimulus duration on behavior

To investigate whether short bursts of stimulus presentations induces a motion percept with behavioral consequences, random dot motion of a reduced set of coherences (0.3, 0.6 and 1) were presented as pulses of varying durations, ranging from 1 s to 10 s (Figure 3.4a and Methods section 2.2.3). Each stimulus was preceded and followed by 6 s of coherence 0 (random motion), to prevent any potential influences from previous trial coherences. As shown in Figures 3.4b and 3.4c, turning rate depends on the time that the coherence-based stimulus has been shown: 1 s of coherent motion stimulus is enough to induce an increase in fish turning rate in the direction of the perceived motion. This is apparent both in the 1 s pulse duration trial, as well as in the longer duration trials, where turning rate increase starts around 1 second following trial onset. As opposed to the randomized coherence experiment where different coherences immediately followed one another, here, the turning rate increase could be attributed only to the current trial coherence (since the trial was preceded by random motion). Following trial end, the increased turning rate persists for at least 1 s for shorter pulse durations (Figure 3.4b, for example, coherence 0.6, 2 s pulse). With increasing pulse duration, the turning rate increase is enhanced, and prolonged throughout the duration of the stimulus, including up to 2 seconds following the coherent motion stimulus (for example, coherence 0.6, 10 s pulse). This effect is more pronounced with coherences 0.6 and 1, however, the same pattern is apparent with coherence 0.3 as well. This behavior is consistent with a temporal accumulation of evidence but is not consistent with a fixed time delay between sensory stimulus and motor output: even if the stimulus set a stochastic mechanism to generate bouts, one would observe a discrete jump in the behavioral turning rate occurring when the rate parameter

change was implemented, and not a gradual change in turning rates. These results also show that the evidence accumulated is not reset when performing a bout, suggesting that sensory and/or motor history affect behavioral performance.

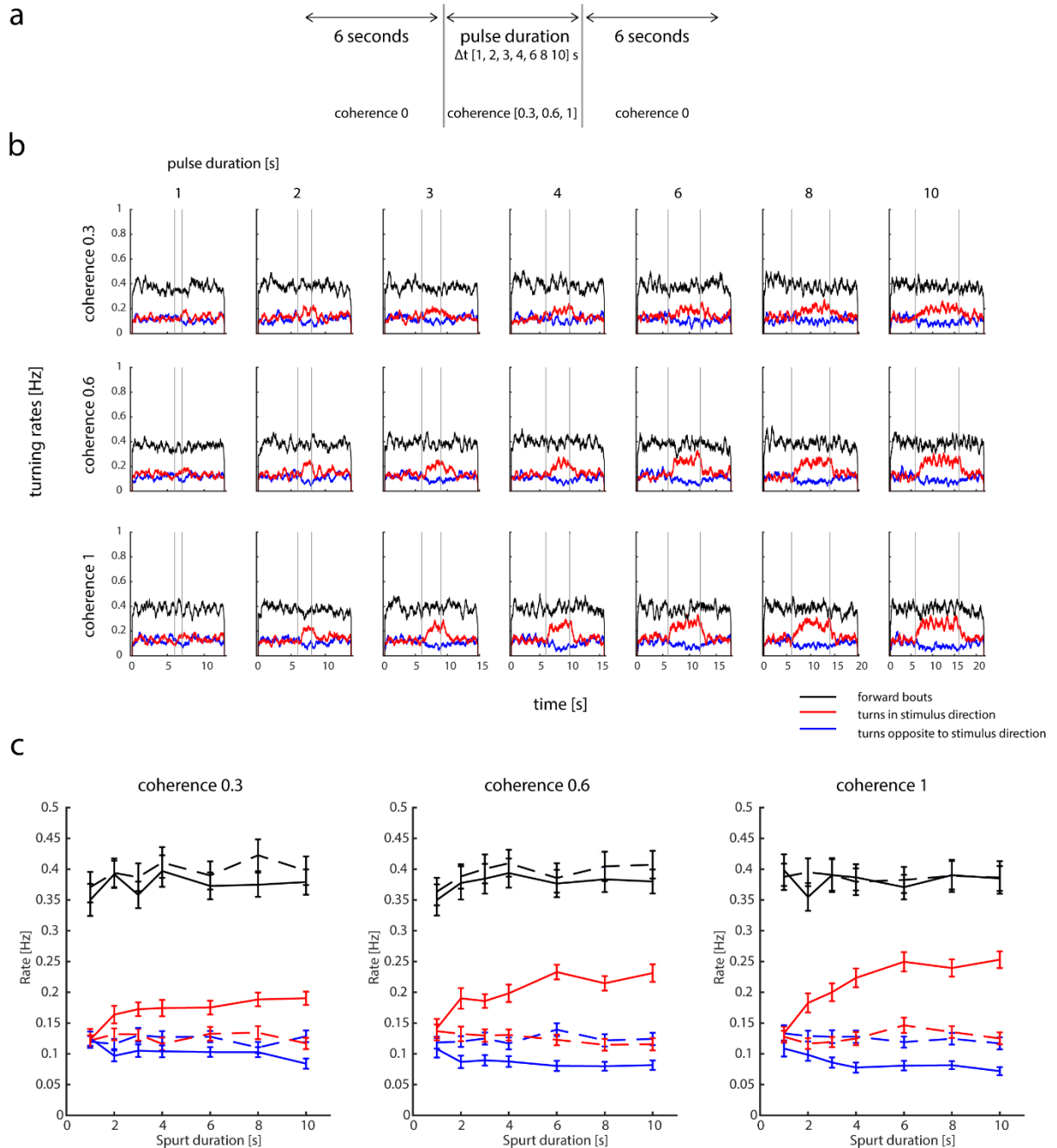


Figure 3.4 Turning behavior with various stimulus duration

a, Schematic of experimental paradigm involving stimulus pulses. 6 seconds of coherence 0 were followed by a pulse coherence 0.3, 0.6 or 1. The stimulus pulse lasted 1, 2, 3, 4, 6, 8 or 10 seconds. After the pulse is over, 6 seconds of coherence 0 were presented again. **b**, Forward swimming and turning rates for the three different coherences and the seven different pulse durations presented. The vertical gray lines denote pulse start and end. Instantaneous rates were computed by averaging over a 200 ms window. **c**, Average behavioral rates for forward swimming (black), turning in the direction of the stimulus (red) and against the stimulus (blue) averaged over the whole pulse as a function of the total pulse duration. In dotted lines the average baseline rates are shown computed over the 5 second window from second 1 to second 6 right before pulse onset (see panel a). Error bars denote SEM (N=54 fish). *Figure adapted from Dragomir et al. (under review)*

3.3 Sensory and motor history affect behavioral choice

Having observed that turning rate increase is persistent following trial offset, turning behavior was further analyzed to investigate whether it depended only on the current stimulus or whether it displayed any dependence on either the previous stimulus shown or the previous motor output produced. Fixed transition experiments were acquired with a reduced set of coherences (0.3, 0.6 and 1) - with trials such that every coherence transition was probed an equal number of times (see Methods section 2.2.3 for details). Dividing all trials for a given coherence according to the previous coherence showed that the turning behavior depends not only on the current coherence, but also on the direction (and not the magnitude), of the previous coherence (Figure 3.5a). This effect is particularly noticeable after trial transitions of opposite direction coherences, where fish exhibit an inertia like behavior and only start turning in the correct direction after about two seconds. This could be due partly to a delayed initiation of turning in the current trial, and as Figure 3.5b shows, the latency to the first correct turn in the current trial is indeed higher for the

trials in which the previous coherence was in the opposite direction. The inertia following trial transitions of opposite coherence directions could also arise due to increased likelihood to turn in the direction of the previous coherence (Figure 3.6b).

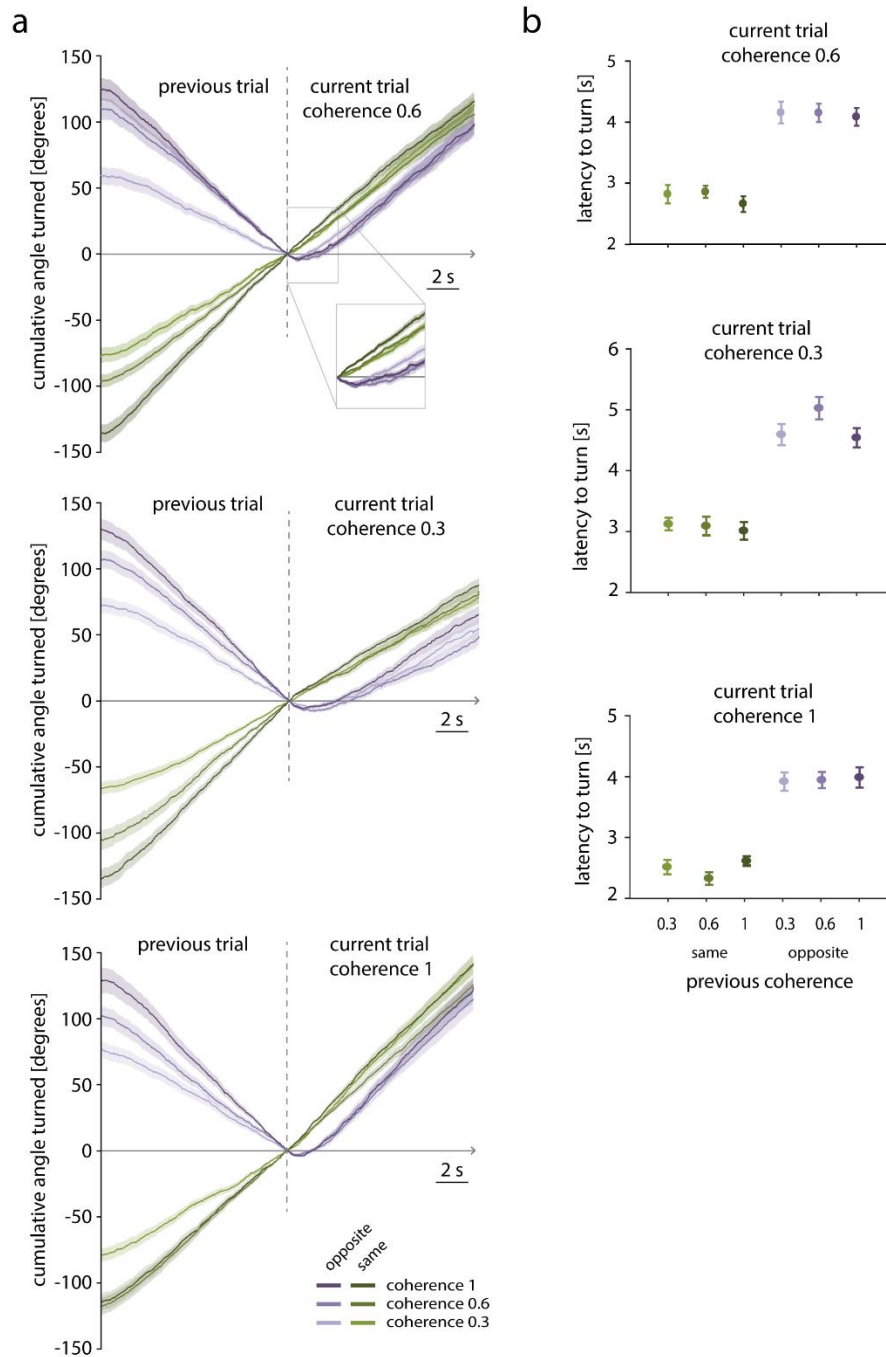


Figure 3.5 Turning behavior is dependent on sensory history

a. Turning behavior during trials of coherence 0.6, 0.3 and 1 as a function of the coherence presented during the preceding trial. Trajectories are split by both magnitude and direction of the preceding trial. **b.** Latency to first correct turn in trials of coherence 0.6, 0.3 and 1, as a function of the coherence of the preceding trial. Negative coherences indicate previous coherence in the opposite direction and positive coherences indicate previous coherences in the same direction as the current trial coherence. (N=50 fish, 18964 trials, 166059 bouts). All error bars and shaded intervals denote SEM. *Figure adapted from Dragomir et al. (under review)*

To investigate whether this history dependence comprised both a sensory and a motor effect, trials were further divided in which the current coherence was the same into four categories depending on whether the coherence and the last bout in the previous trial was in the same or opposite direction. Trajectories elicited by the same stimulus transition differed significantly from each other during the current trial, depending on whether the previous motor output had been in one or the other direction. The same inertia-like behavior was also present if only the turn preceding the stimulus transition was in the opposite direction, even if the stimulus direction remained the same (see for example red solid and dotted lines in Figure 3.6a). In addition, the fraction of correct first turns showed a similar dependency on previous motor output (Figure 3.6b). To describe and quantify the sensory and motor influences, a multivariate logistic regression model was constructed that defines the likelihood of observing a left versus a right turn based on both the coherence shown during previous bouts and the direction turned (see Methods section 2.5.1 for details). As shown in Figure 3.7, the significant sensory coefficients extended from the current to the previous three bouts, while the significant motor coefficients included the previous four bouts (this was consistent across fish, data not shown). Overall, the analysis shows that both sensory and motor history influence the current behavioral choice, corroborating results found in other decision making studies using primates and rodents (Gold et al., 2008; Roitman and Shadlen, 2002; Hwang et al., 2017; Akrami et al., 2018; Scott, Constantinople et al., 2017).

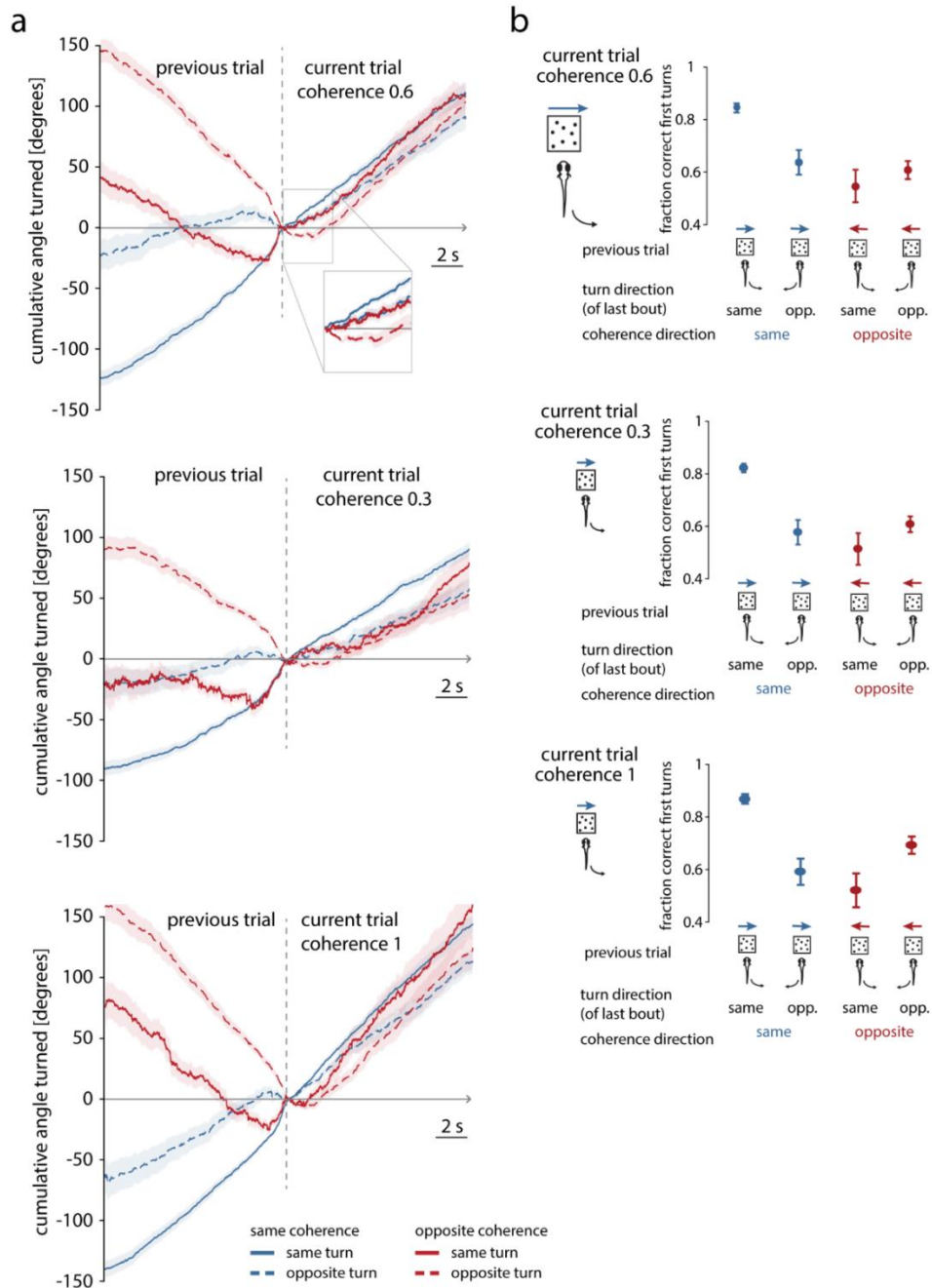


Figure 3.6 Turning behavior is dependent on motor history.

a. Turning behavior during trials of coherence 0.6 as a function of both the direction of the coherence presented during the preceding trial and the

direction of the last turn in the preceding trial. Only preceding trials with coherence of magnitude 0.6 were included. **b.** Fraction of correct first turns during trials of coherence 0.6 as a function of both the direction of the coherence of the preceding trial and the direction of the last turn in the preceding trial. Only preceding trials with coherence the same magnitude as the current trials were included. (N=50 fish, 18964 trials, 166059 bouts). All error bars and shaded intervals denote SEM. *Figure adapted from Dragomir et al. (under review)*

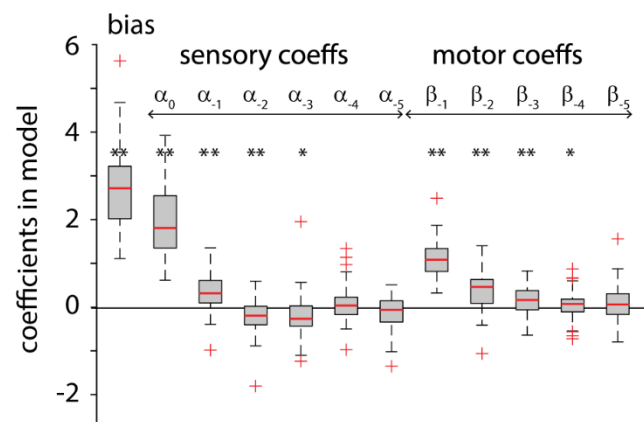


Figure 3.7 Sensory and motor history effects on behavior

Values of coefficients for multivariate logistic regression model averaged across fish (see Methods for details). α_n corresponds to the coherence presented during the n-th previous bout and β_n to the behavior of that bout. Red lines denote medians, boxes encompass 25th and 75th percentiles and crosses denote outliers. Asterisks denote the coefficient is significantly different from 0 (Wilcoxon signed rank test $p < 0.05$ and $p < 0.001$). (N=37 fish, 5688 trials, 126754 bouts). Red lines denote medians, shaded regions encompass from the 25th to the 75th percentile, whiskers encompass all non-outlier points and red crosses denote outliers. The only significant

values found were $K=2.76$, $\alpha_0=1.96$, $\alpha_1=0.36$, $\alpha_2=-0.22$, $\alpha_3=-0.17$, $\beta_1=-0.97$ and $\beta_2=-0.34$, $\beta_3=-0.20$, $\beta_4=-0.09$ (these medians are: 2.66, 2.01, 0.40, -0.22, -0.18, -0.97, -0.42, -0.22, -0.10). The motor coefficients were multiplied by -1 to coincide with the direction of the sensory coefficients.

Figure adapted from Dragomir et al. (under review)

3.4 Whole-brain imaging uncovers neuronal correlates

In order to locate the neural correlates related to the decision making process underlying turning, the freely swimming assay was adapted to a preparation in which the larval zebrafish was head restrained yet able to move its tail (Portugues, Feierstein et al., 2014), while it was being shown a reduced set of coherence stimuli (see Methods section 2.4.2 for details). This allowed for monitoring both neuronal activity and behavioral output in a trial-by-trial basis. Although the behavior observed was not as reliable as in the freely swimming assay, it still showed a clear lateralization dependent on the stimulus shown (Figure 3.8c), and the psychometric curves for both the fraction of correct turns as well as the latency to the first correct turn (Figure 3.9), mimics the ones observed in the freely swimming setup (Fig. 3.3b).

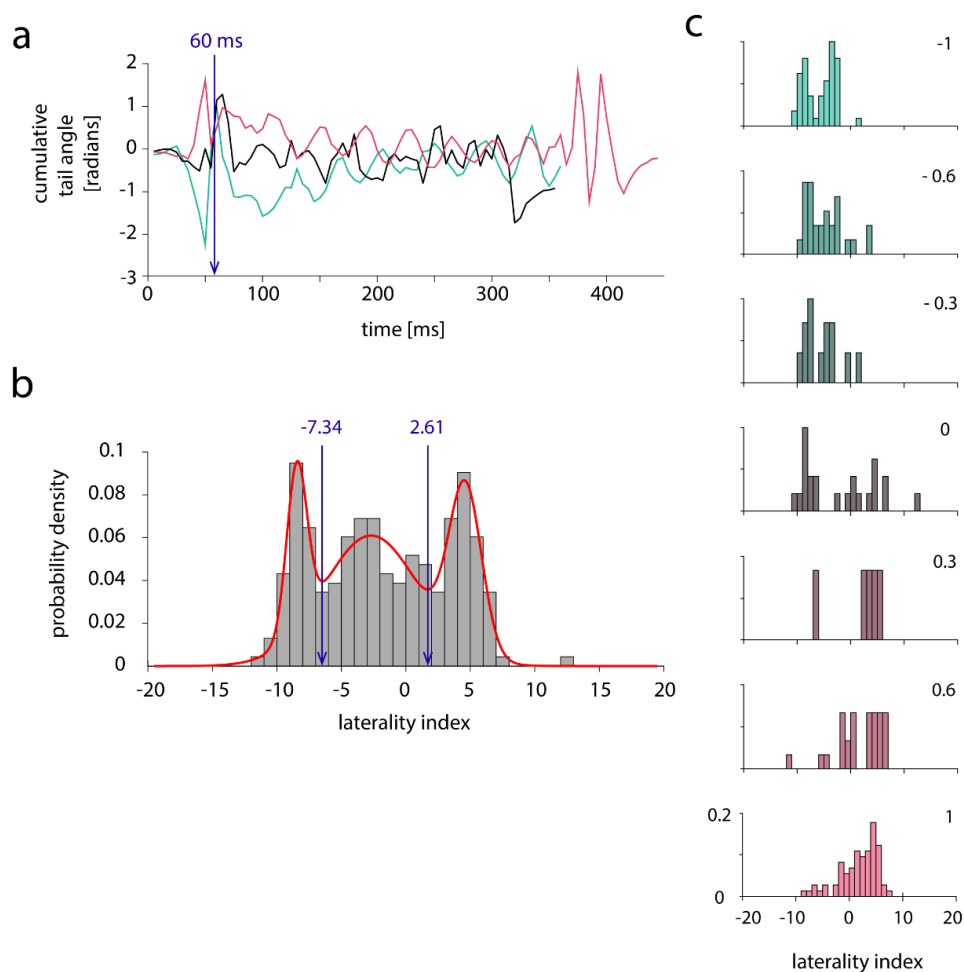


Figure 3.8 Tail tracking and bout categorization in head restrained experiments

a. Average tail traces of all bouts elicited during presentation of stimuli with coherence +1 (red), 0 (black) and -1 (green) for one example fish. Leftward turns, forward swims and rightward turns, which are the predominant behaviors during these stimuli presentations, can be clearly distinguished by computing the sum of the cumulative tail angle during the first 60 ms of the bout, which is referred to as the laterality index. **b.** Histogram of all laterality indices for the example fish in **a**, showing a distribution with three peaks corresponding to left- and right-ward turns and forward swims. Thresholds can be imposed to distinguish between these behaviors, in this case -7.34 separates rightward and forward swims and 2.61 separates

forward swims and left-ward turns. **c.** Individual histograms for all bouts elicited during stimulus presentations of the different coherences for the sample fish in a. *Figure taken from Dragomir et al. (under review)*

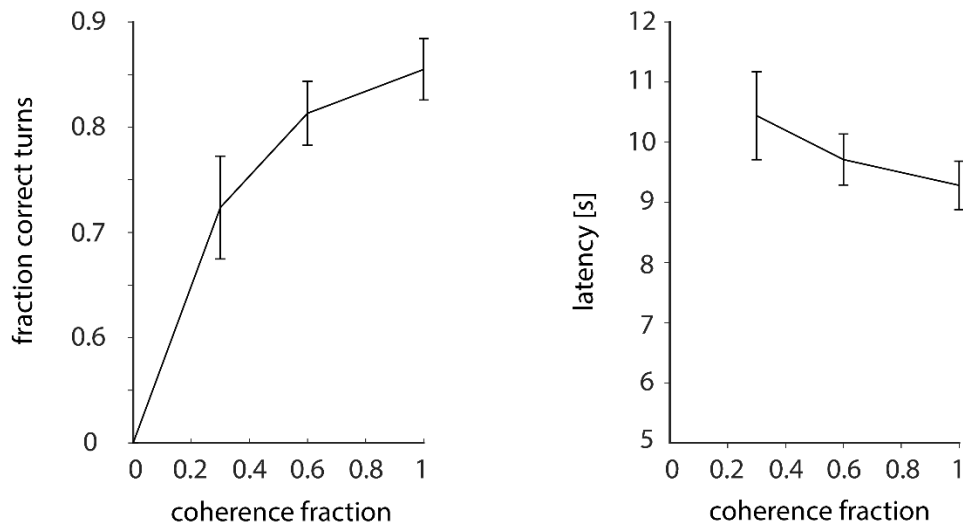


Figure 3.9 Head restrained turning behavior depending on coherence

Left: Average fraction of correct turns (in the direction of presented coherence). Right: Average latency (time from stimulus onset) to first correct turn as a fraction of stimulus coherence. Averages over N=18 fish; error bars denote SEM. *Figure adapted from Dragomir et al. (under review)*

The brains of 22 animals were imaged comprehensively under a scanning two photon microscope (Figure 3.10). The raw data was processed to remove motion artifacts, identify and segment active neurons based on local correlations in an unbiased way (see Methods section 2.4). All units were registered to a reference brain and their ROIs included in all further analysis (a total of 2,170,552 ROIs in 22 fish).

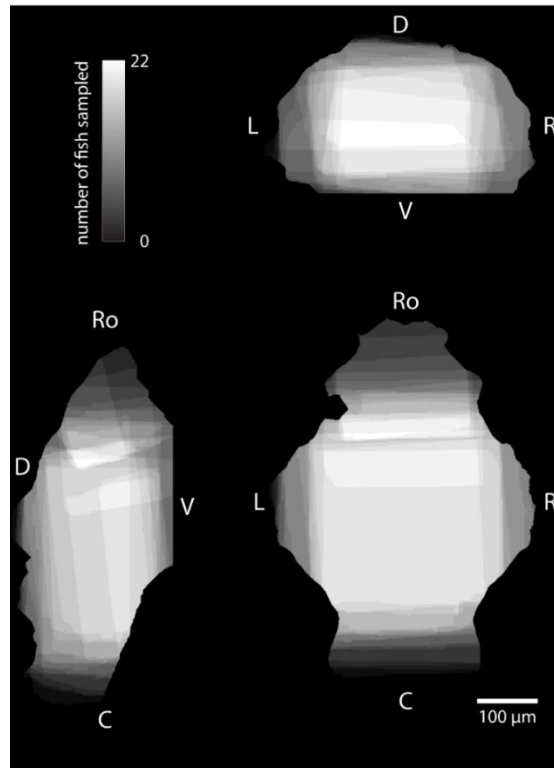


Figure 3.10 Brain regions sampled during imaging experiments

Sum of projection footprints along the three axes for all brains that were imaged and could be registered to the reference brain. *Figure adapted from Dragomir et al. (under review)*

Regressors were built to identify whether any of the neurons had signals that could be associated to the decision making process, which was regarded as a three step process consisting of: (i) the transformation of the sensory stimulus into a momentary sensory drive, (ii) the integration of this sensory drive in time as accumulation of evidence and (iii) a threshold-crossing stage resulting in the behavioral choice (Figure 3.11a). For signals that correlated with the presence of visual motion (irrespective of the direction), the coherence (motion strength) of the stimulus, and the integration of this sensory evidence in time, either unilaterally or bilaterally, regressors were built from the sequence of the coherence stimulus. For motor related signals, regressors were built from the analysis of the recorded

tail motion (for details see Methods section 2.3.4). The full list of regressors is displayed in Figure 3.11b.

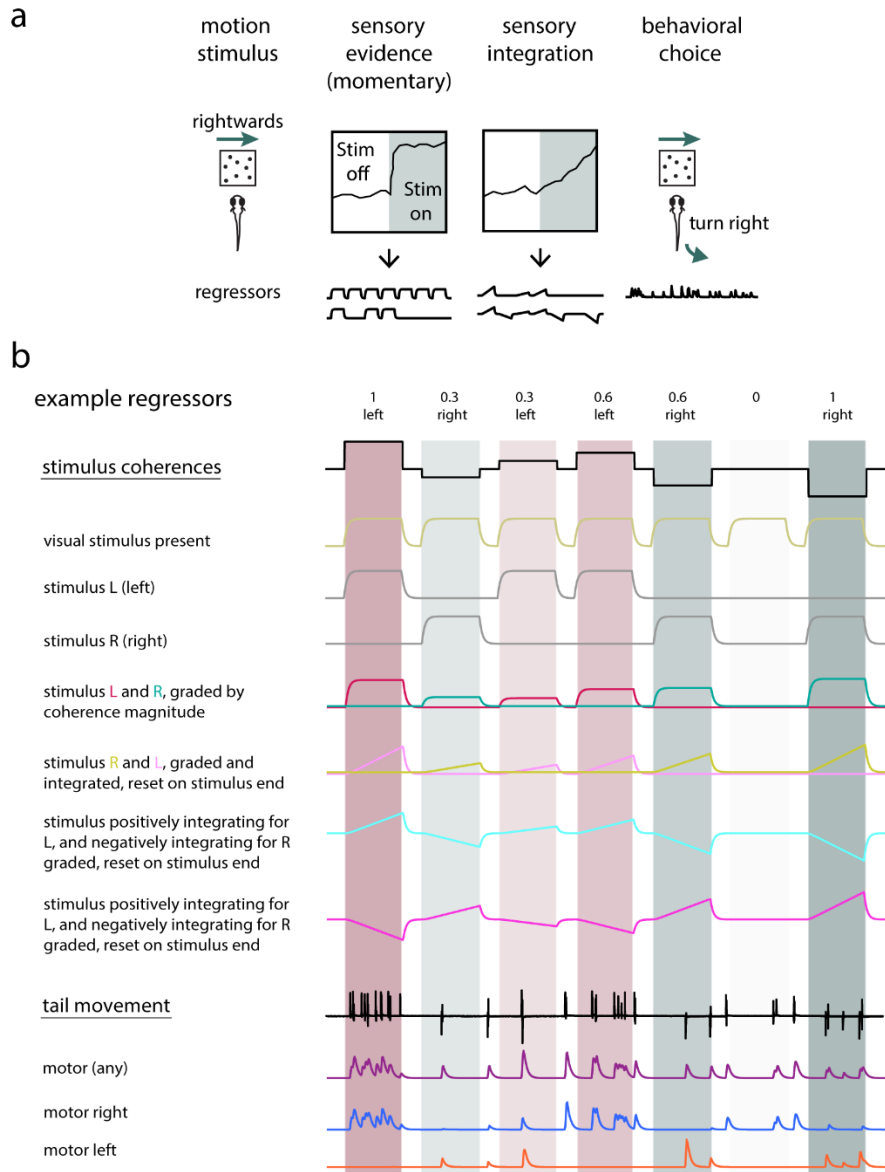


Figure 3.11 Regressors used in whole brain imaging experiments

a. Schematic of the decision making steps, and some potential corresponding regressor examples. **b.** full list of regressors; the regressors are constructed from

the stimulus coherence shown and the tail movement recorded (both underlined) *Figure adapted from Dragomir et al. (under review)*

Interestingly, neural activity in the majority of the brain regions imaged were found to correlate with a particular variable of the decision making process. Figure 3.12 shows the ROIs that correlate above a set threshold with the regressors analyzed, and Figure 3.13 displays some example traces of ROIs, whose activity correlates well with the regressors indicated. The ROI traces are taken from different brain areas (displayed in the reference brain projection in figure 3.13a) and all traces belong to ROIs that span at least 5 planes, therefore they were exposed to 5 repetitions of each coherence stimulus. The anatomical distribution of ROI types displayed in Figure 3.12 was very consistent across all the fish.

The presence of visual motion, irrespective of direction or stimulus magnitude, was almost exclusively represented in the activity of the optic tectum neuropil area (Figures 3.12 and 3.13b, top fluorescence trace).

Signals that were graded according to the coherence magnitude were found in multiple areas, including the dorsal left habenula, pretectum, dorsal thalamus, tegmentum, reticular formation and DRN (Figures 3.12 and 3.13). Except for the habenula and optic tectum, left- and rightward visual motion was lateralized and located on the left and right side of the brain, respectively.

In addition to typically fast rising responses that are graded by coherence, present mostly in the pretectum and reticular formation, some ROIs show integrating-like activity patterns, with slower rises, that are also dependent on the coherence magnitude. These tend to be clustered more medially and dorsal in the pretectum, dorsal thalamus and torus longitudinalis in the midbrain, habenula in the forebrain, and more laterally in the reticular formation, DRN and IPN in the hindbrain (Figures 3.12 and 3.13). Interestingly, the habenula, DRN and IPN, which are anatomically connected (reviewed in Bianco and Wilson, 2009), also show a different category of stimulus related responses, integrating activity in a bidirectional manner: excitation for the preferred direction and inhibition for the opposite direction. As shown explicitly in Figure 3.13b, the integrating signals

described do not arise from averaging step responses across multiple trials, but are already present at the level of individual trials.

Motor related ROIs corresponding to acute directional turns were also lateralized, and found in the reticular formation, lateral parts of the dorsal raphe nucleus, tegmentum, and in the caudal part of the hindbrain (Figures 3.12 and 3.13b, bottom traces).

It is interesting to note that several of these areas contain multiple types of ROIs. In the anterior hindbrain region of the reticular formation for example, there were signals with both fast rising activity profiles and integrating ones, depending on the coherence magnitude and direction showed, as well as acute motor responses correlated with directional turning behavior. In the dorsal left habenula, DRN and IPN, ROIs with integrating activity display various ratios of excitation and inhibition. For example, the first traces from the habenula and DRN (from the integrated graded signals category) show mostly excitation during rightward motion coherence, while the second traces (from the bidirectional integration category) have a combined activity pattern, with excitation to rightward motion and a more pronounced inhibition from leftward motion. In a similar way, the first example trace from the IPN shows mostly inhibitory activity during rightwards motion, while the second trace has a combined excitation during rightward motion and inhibition during leftwards motion.

While these directional visual motion signals were expected in some of these areas, for example in the pretectum, in agreement with previous studies that have shown similar activation in response to wholefield visual motion (Portugues, Feierstein et al., 2014; Kubo et al., 2014; Naumann et al., 2016), in regions such as the dorsal left habenula, DRN, IPN, no such neural responses have been previously identified. In the medial anterior region of the hindbrain, graded sensory responses were found in regions previously identified with turning motor activity (Huang et al., 2013; Dunn et al., 2016; Wolf et al. 2016).

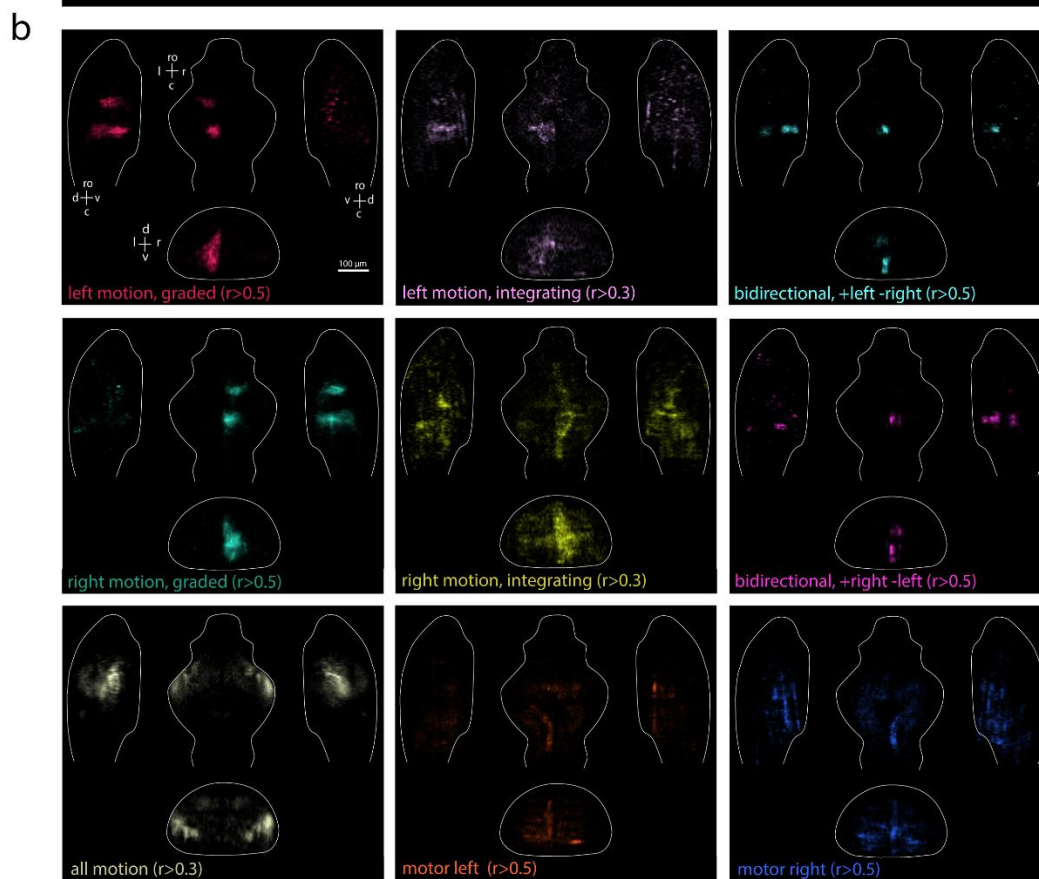
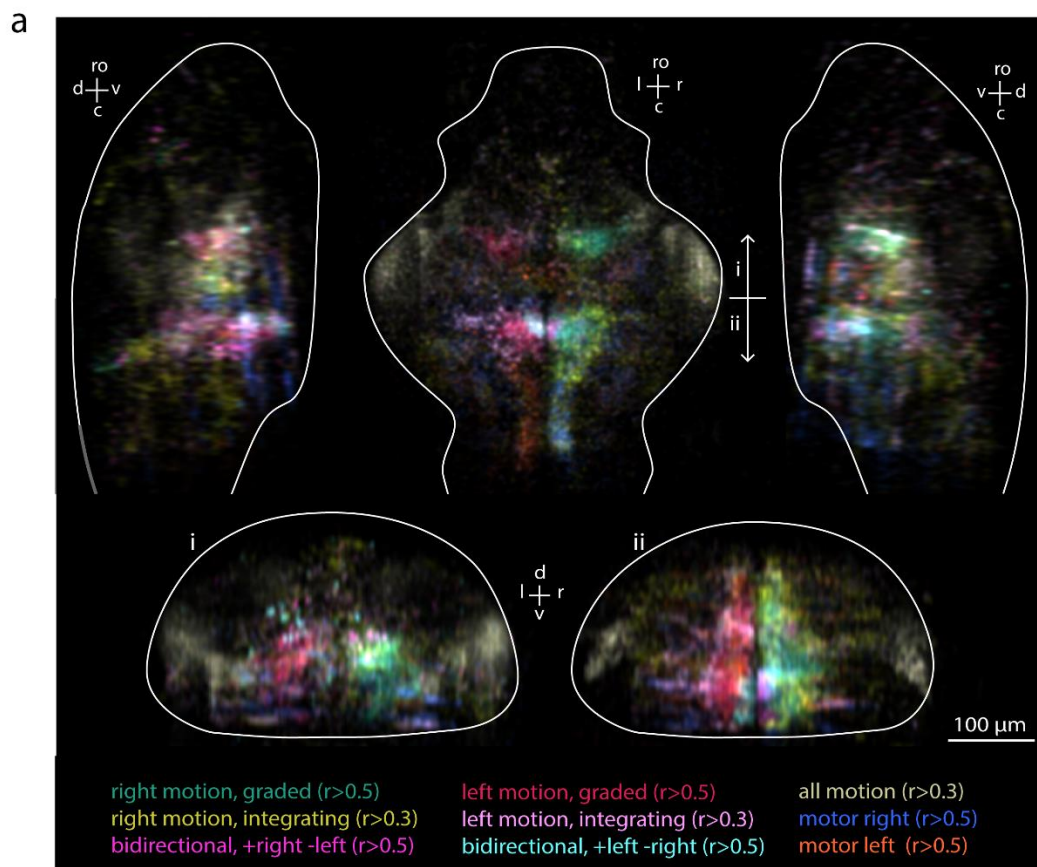
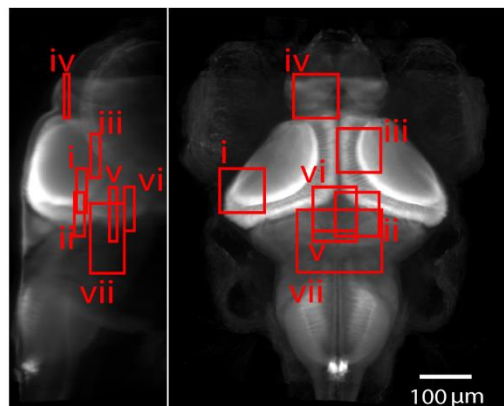


Figure 3.12 Whole-brain ROI maps color coded according to various sensory and motor related regressors

a. Top: views from lateral left (left), dorsoventral (central) and lateral right (right) ROI projections. i) and ii) show medial views corresponding to rostral and caudal parts of the zebrafish brain, respectively. Each regressor and corresponding correlation thresholds for ROIs shown here are displayed at the bottom. **b.** ROI maps color coded according to individual sensory and motor related regressors displayed in **a**. Each map has views from lateral left (left), dorsoventral (top central), lateral right (right) and rostro-caudal (bottom) ROI projections. *Figure adapted from Dragomir et al. (under review)*

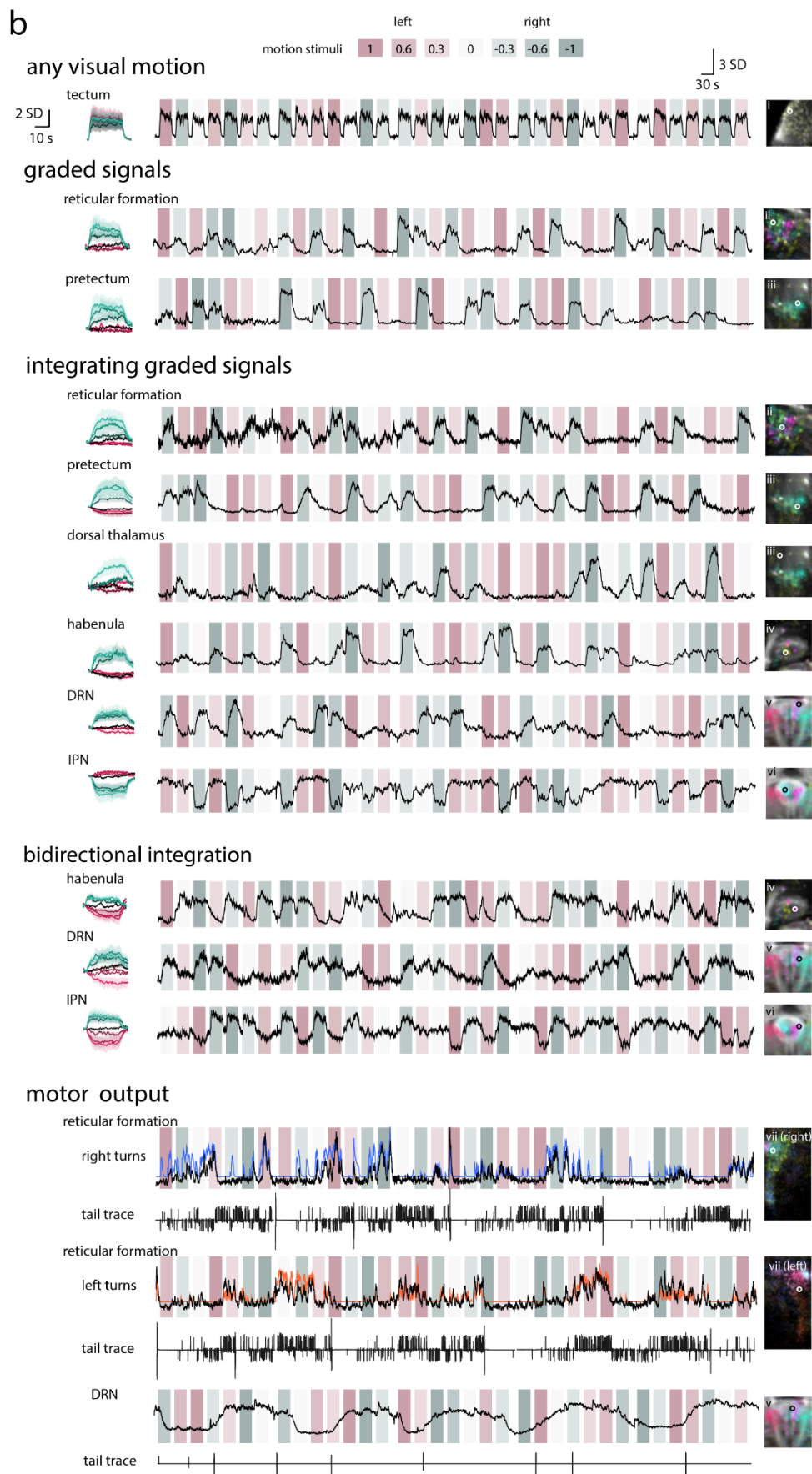
a



- i - optic tectum
- ii - reticular formation
- iii - pretectum, dorsal thalamus
- iv - habenula
- v - DRN
- vi - IPN
- vii - reticular formation, DRN

Figure 3.13 Neural correlates of the decision making process and their anatomical distribution (continued on next page)

a. Reference brain with location of each anatomical inset and its representative trace displayed in **b**; **b.** ROI types in six different brain regions with representative raw traces (in black) spanning at least five planes. For the motor ROIs, the corresponding regressor (right and left turns in blue and orange, respectively) and tail trace (arbitrary units with positive upward deflections denoting leftward turns) are also displayed. Shaded intervals throughout denote SEM. *Figure adapted from Dragomir et al. (under review)*



3.5 Mapping a decision making model to the neuronal data

Theoretical frameworks proposed to understand this decision making process involve two integrators, one for each of the possible behavioral choices, which accumulate corresponding evidence in support of that particular choice (Bogacz, 2007). These integrators may solely accumulate ipsilateral momentary sensory evidence or in addition, may be inhibited by either contralateral momentary sensory evidence (the feed-forward inhibition model or FFI, Shadlen and Newsome, 2001) or the opposing integrator (leaky competing accumulator model or LCA, Usher and McClelland, 2001). A reliable distinction between these two architectures is not possible within the experimental paradigm used (both models fit the data equally well), so a general model architecture based on FFI was defined to describe individual ROI responses. The model describes the activity of an ROI as the sum of leftward and rightward sensory streams. In each stream, the visual processing that leads from partially coherently moving dots to momentary sensory evidence is modeled as a power nonlinearity. This is subsequently integrated by units with time-constants that are independent for the left and right streams and summed with weights that can be either positive or negative (Figure 3.14a and Methods section 2.5.2). This model can describe units that respond equally to all motion directions, units that respond to unidirectional motion in either a graded or an ungraded way, and units that integrate either uni- or bi-directional motion positively and/or negatively (Figure 3.14b). This model was fitted to the activity of every individual ROI, and the goodness of fit was used to identify all brain regions that were correlated with the decision making process (Figure 3.14d). Notably, this analysis was able to pinpoint relevant neuronal activity to a few anatomical locations that are described below.

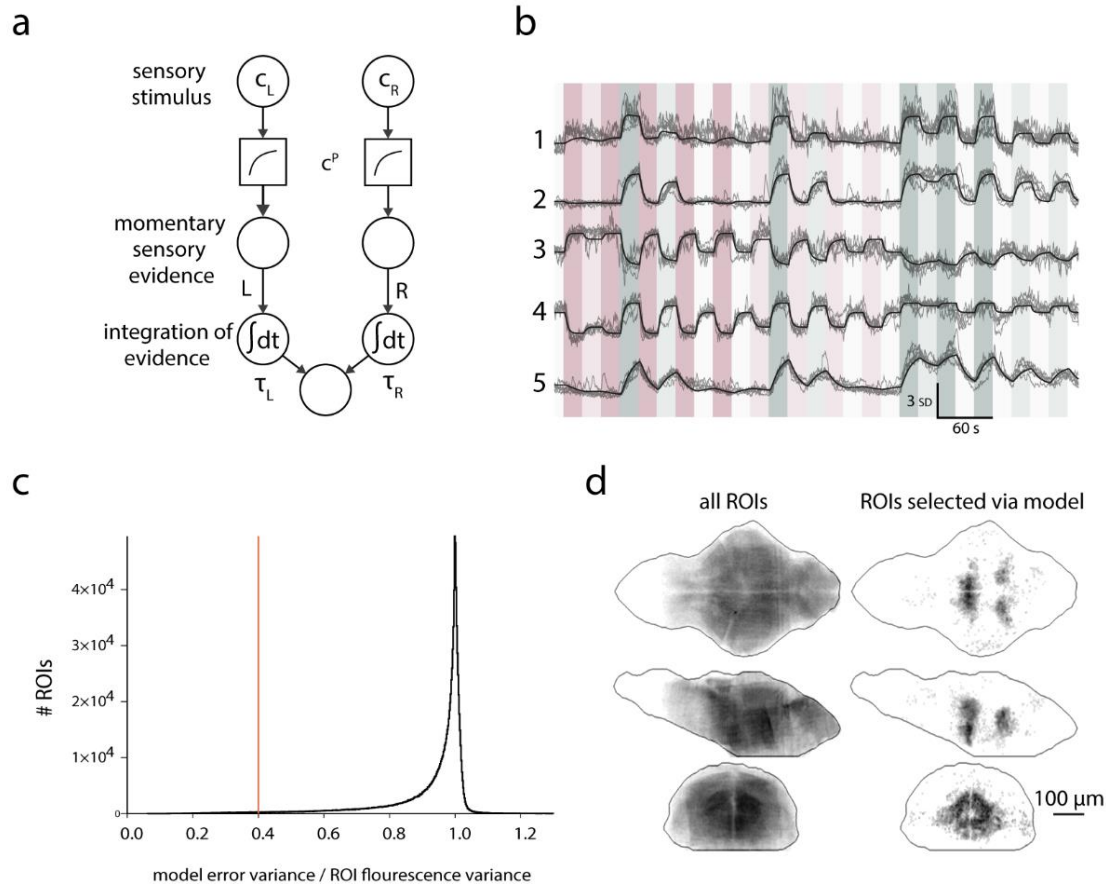


Figure 3.14 Fitting a general integrator model to the neural data

a. Schematic depicting model architecture, incorporating previously suggested models within its parameter space. **b.** Sample traces showing fits to neural activity from different parts of the model parameter space; the explained variance for each trace is (in order): 0.612, 0.813, 0.734, 0.790, 0.827. **c.** Variance of ROIs explained by the model. The orange line is the cut of threshold for ROIs displayed in **d**, chosen empirically to discard spurious fits due to artifacts. **d.** Out of the 1,142,100 units, over 70% of the variance in the activity of 8953 is described by the model. *Figure adapted from Dragomir et al. (under review)*

From the five parameters (the power of the nonlinearity, the weight and time constant for each side), two derived parameters were investigated, namely the relationship between response to the two motion directions, expressed as an angle in the weight plane and the dominant time constant (defined as the sum of the two integrator time constants weighted by the input weights) (Figure 3.15a). This analysis revealed a continuum of time constants that extended all the way into the tens of second. Interestingly, the widest range of time constants, including the longest ones, belonged to ROIs that were strongly excited by motion in one direction and slightly inhibited by motion in the opposite direction (between $\pi/2$ and $3\pi/4$).

As each ROI was fitted independently, the anatomical distribution of the fitting parameters throughout the brain of the larval zebrafish was also analyzed. As shown in Figure 3.15 b-d, most units of relevance were found in the pretectum, thalamus, the hindbrain region around the reticular formation and the ventral hindbrain corresponding to the DRN and the IPN, in agreement with the regression based analysis shown in Figure 3.13. Responses dominated by contralateral inhibition were located almost exclusively in the DRN, IPN and dorsal left habenula (pink ROIs in Figure 3.15 b-d). As shown in Figure 3.15d- ii, responses in the pretectal region exhibit a continuous gradation from lateral/ventral responses corresponding to some bidirectional but mostly unidirectional excitation, to medial and dorsal responses that include modest contralateral inhibition. In agreement with Figure 3.12, units that were more excited by right- or leftwards motion were almost uniquely found on the right/left hand side of the brain, respectively (Figure 3.15c).

ROIs with long time constants (> 5 s) were located in several brain regions (Figure 3.15e), including the dorsal and lateral hindbrain around the reticular formation and more ventrally in the DRN and IPN (Figure 3.15e- i), the dorsal pretectum (corresponding to those units that included slight contralateral inhibition), torus longitudinalis and habenula (Figure 3.15e- ii). Notably, this is a comprehensive map: no other units throughout the brain exhibited activity related to visual motion in this experimental paradigm. These ROIs must therefore underlie the coherence-dependent behavior observed and described in Figures 3.1 - 3.9.

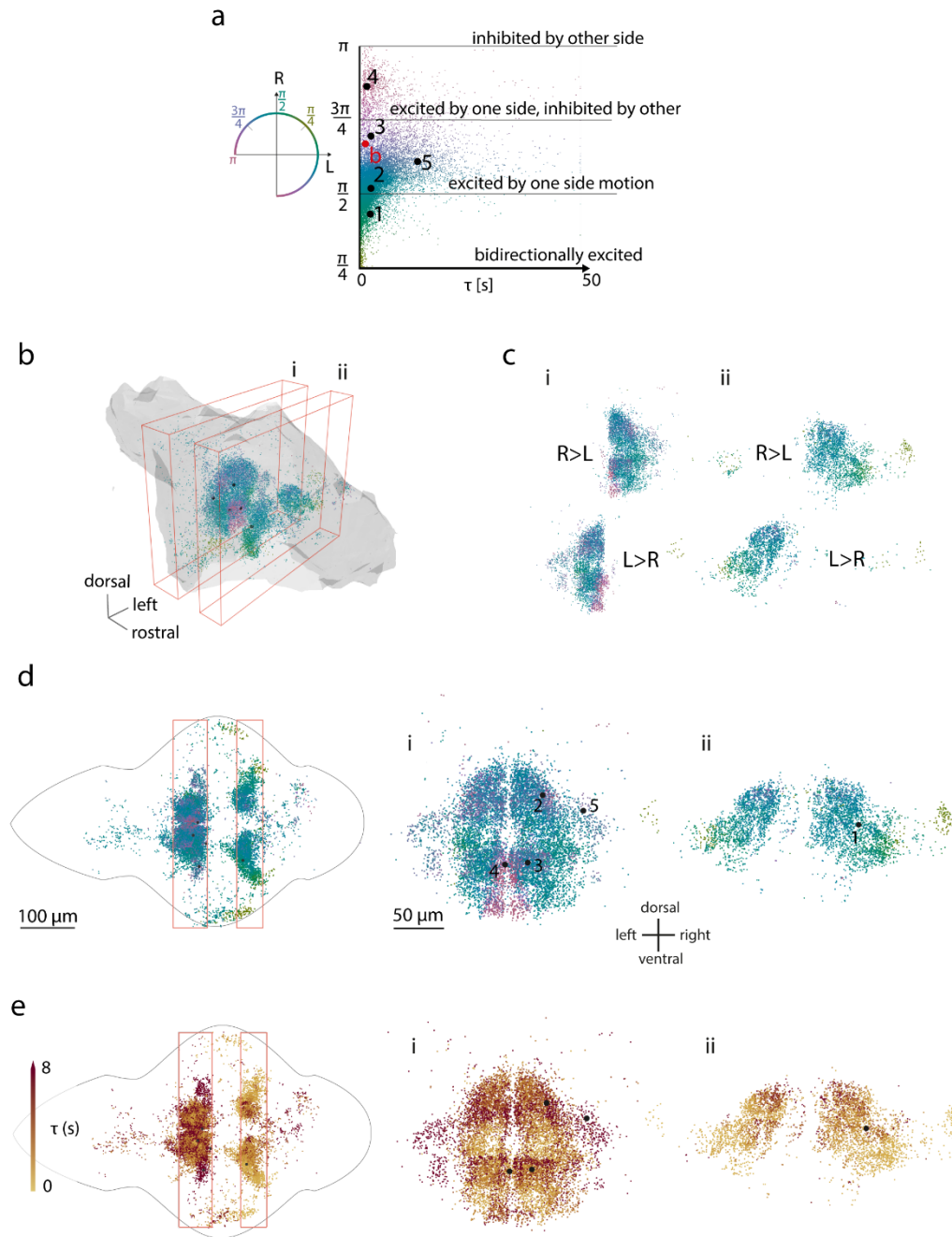


Figure 3.15 Model characteristics and anatomical distribution of fitted ROIs

a. Characterization of the resulting model fits. The x-axis is a sum of the time constants weighted by the absolute values of the left and right weights, and the

y-axis is the amount of inhibition vs. excitation for the dominant side (for details see Methods section 2.5.2). The parameters for the ROI traces shown in Figure 3.12 b are labeled 1 through 5. **b.** 3D anatomical map of model parameters: the colors are from panel **a**, showing regions where ipsilateral excitation or contralateral inhibition dominate. Two transversal slices of the brain volume containing most of the relevant ROIs are displayed below: (i) part of anterior hindbrain and (ii) midbrain regions. **c.** Transversal slices already shown in panels d (i) and d (ii), but here ROIs are split into those for which the input when presented with a leftwards stimulus produces more excitation than a rightward stimulus ($L > R$) and vice-versa to depict the pronounced lateralization. **d.** Anatomical map of model characteristics, with same transversal slices displayed in **b**. **e.** Anatomical map of model time constants, with same transversal slices displayed in **b**. *Figure adapted from Dragomir et al. (under review)*

3.6 Generation of motor output

The ROIs described up to now relate to sensory evidence and its integration. As shown in Figure 3.3c and expanded upon in Figure 3.4, the evidence integrator is not reset upon performing a turn. The question remains as to how the integrated evidence actually influences turning. It has been shown before (Portugues et al., 2015) that the initiation of forward swims when presented with optomotor stimuli of varying speeds can be to a certain extent modeled as a Poisson process, whose rate is a function of the stimulus speed. In the present behavioral paradigm, a similar mechanism was tested by using the left and right integrator values as linear modulation of the rate of two independent Poisson processes that generate left and right turns respectively. As shown in Figure 3.16a, two integrator units (already described in Figure 3.14a, but now setting τ_L and τ_R to be equal) were combined to encode the left and right turning rates respectively (λ_L and λ_R), superimposed on a tonic baseline turning rate λ_B (0.11 Hz). The model was fit to reproduce the behavior observed

during one of the two behavioral paradigms tested and the synthetic trajectories generated show both qualitative and quantitative similarities to those found experimentally (see Methods section 2.5.2 and Figure 3.16b). The values obtained for the model were a time constant, $\tau = 0.96$ seconds and a turning angle per bout = 58.27 degrees (although this value is relatively large compared to an usual turning angle, in this way forward turns that are slightly biased to one direction or another are also accounted for, while keeping the behavioral rate consistent with other experiments). This same model was then applied to predict the turning rate expected during the stimulus sequence (Figure 3.17-i) presented in the imaging setup during which the larvae were head restrained (Figure 3.17-ii) (see Methods section 2.5.3 for details). The freely swimming behavior expected when this stimulus sequence is presented showed a very close agreement with the model (compare Fig 3.17 ii and iii) with very similar deviations from baseline occurring as a function of the coherence presented. For the head-restrained behavior (Figure 3.17-iv) salient behavioral features were also similar, such as the predominant turning direction during each stimulus and relative turning frequencies. Nevertheless, the swimming in head-restrained zebrafish larvae is known to occur at a much decreased rate, which in this model could correspond to a decrease in λ_B and/or a reduced input to the turning integrators. This would result in an overall homogeneous decrease of turning rates (see gray line in Figure 3.17-ii). In addition, the proposed mechanism can also explain why, even for high coherences, fish will sometimes perform an incorrect turn. This is due to the stochasticity of the model and the fact that the baseline turning rate, determined by λ_B , is non-zero for both freely swimming and head-restrained behavior.

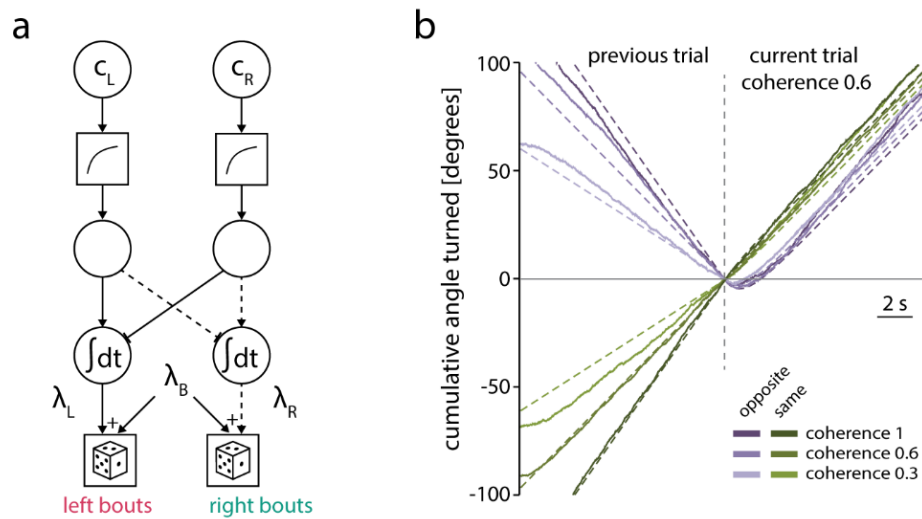


Figure 3.16 Behavioral predictions of motor output generation model

a. Version of the model that relates the evidence integration process to bout generation. **b.** Simulated behavioral response of the integrator model (dashed line) to transitions in coherence and direction superimposed on data shown in Figure 3.5a (for coherence 0.6). The relative weights of excitation and inhibition and the nonlinearity P were extracted from data presented in Figure 3.3a, whereas the time constant was extracted from behavioral data presented in Figure 3.5a. *Figure adapted from Dragomir et al. (under review)*

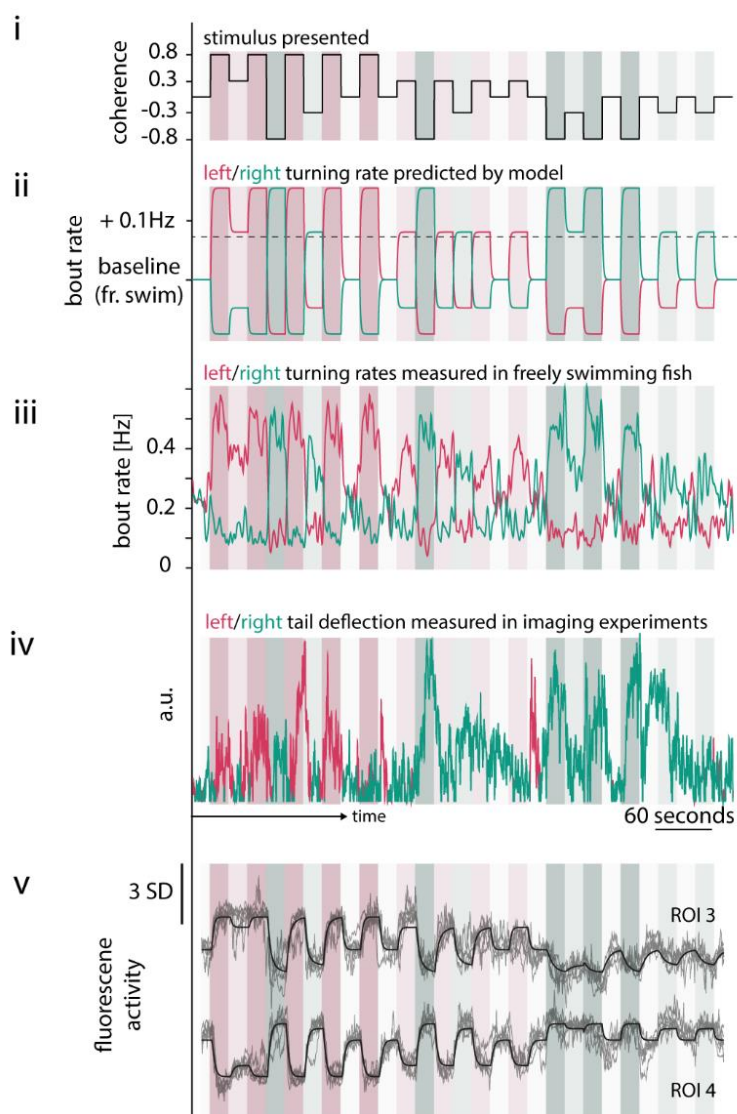


Figure 3.17 Relation of turning rate with model fitted fluorescence

(i) Direction and coherence of the stimulus sequence; (ii) the turning rates predicted in by the model fitted on data from Fig 3.3 and Fig 3.5a; gray line denotes threshold below which turns are not expressed in the head-restrained preparation; (iii) turning behavior in freely swimming fish and (iv) embedded fish; (v) fluorescence traces reproduced from figure 3.14b with similar parameters as the behavioral model. *Figure adapted from Dragomir et al. (under review)*

As shown in Figure 3.17-ii, these units representing the turning rate display positive and negative deviations from a baseline activity depending on whether the sensory evidence coincides or not with the turning behavior they encode. In the parametrization from Figure 3.15a, they must therefore lie around the value $3\pi/4$ and should appear pink in Figure 3.15 b-d, such as ROIs 3 and 4 from Figure 3.14b, which are reproduced at the bottom of Figure 3.17-v. The majority of these ROIs are found in the hindbrain (Figure 3.15d-i). In addition, as already shown in Figure 3.15c, all ROIs that are predominantly excited by leftward coherence are almost uniquely located on the left side of the brain, and similarly for the rightwards coherence. This allows for establishing a functional circuit model (Figure 3.18) where rate encoding units in the anterior hindbrain receive ipsilateral excitatory and contralateral inhibitory inputs that must originate in the pretectum, the only visual sensory region that is active in a coherence-graded fashion. Notably, the circuit model presented in Figure 3.18 is not an anatomical model but a functional one, and that inhibitory inputs to the turning rate encoding neurons could also anatomically arise from neurons in the contralateral hindbrain.

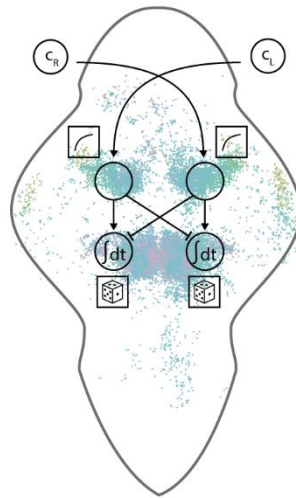


Figure 3.18 Mapping of brain areas to parts of the evidence integration process. *Figure adapted from Dragomir et al. (under review)*

Using the whole-brain imaging dataset as a functional screen, the regions in the medial ventral anterior hindbrain (colored pink in Figure 3.15d-i) were further investigated, since, as pointed out above, they could correspond to the turning rate encoding units. The IPN, a structure located on the midline of the larval zebrafish brain contained the majority of these units. The neural responses in this region were correlated with the left turning rate, and activity was markedly lateralized: in the caudal IPN, activity on each side was highly correlated for ipsiversive turns and anticorrelated for contraversive ones, whereas this pattern was switched in the more rostral IPN (Figure 3.19). This is confirmed by partitioning this region into six segments: deviations from baseline in the activity in the pink segment closely tracks the deviations from baseline in right turning rate (cf with Figure 3.17 ii-iv), and similarly for the green segment and left turns.

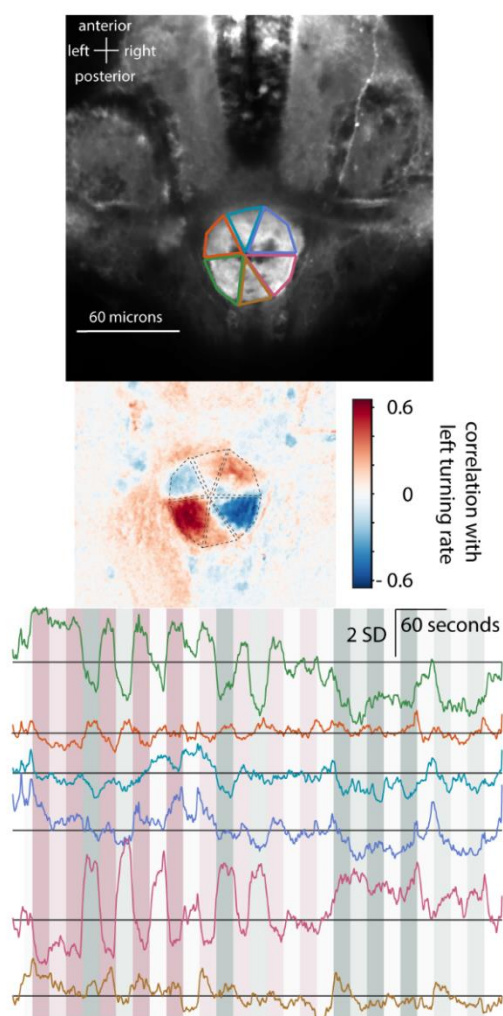


Figure 3.19 Activity in the IPN correlates with the integrated sensory evidence and directional turning rate

The anatomy showing the location of the IPN (top); 6 regions selected from the pixel-wise correlation (middle) with modeled left turning rate (the pink trace in Figure 3.17-ii). Bottom: example traces from the 6 segments selected in the above panels. *Figure adapted from Dragomir et al. (under review)*

To further investigate how turning rates are transformed into motor output, motor-triggered neuronal activity averages (MTNAs) were computed for all the ROIs identified in the behavioral analysis from the imaging experiments. A set of activity profiles of interest were defined for the three behaviors observed, namely left and right turns and forward swims, referred to as motor triggers (Figure 3.20 - for simplicity only left turns are displayed, except in e). For example, the triggers in Figure 3.20a correspond to neuronal activity that increases or decreases in a step-up fashion upon motor output. The trigger in Figure 3.20d corresponds to neuronal activity that starts ramping down several tens of seconds before a motor event after which it is instantaneously reset, while the trigger in Figure 3.20e corresponds to neuronal activity concurrent with a motor event, such as would be expected from a motor neuron. The activity of each individual MTNA was correlated with these motor triggers and only ROIs that had a high correlation coefficient (> 0.7) were selected. The motor trigger corresponding to integrated activity that is reset upon motor output was omitted, as no significant number of ROIs with such MTNAs patterns were found (this would correspond to the inverse of the trigger in Figure 3.20d). Analyzing ROIs with significant leftward turning MTNAs (Figure 3.20a-d), revealed functional classes corresponding to different activity patterns, which were anatomically lateralized: for each pair, the ROIs with the green trigger were mainly located on the right side of the brain while those with the magenta trigger, which perfectly anticorrelates with the green trigger, were located on the left side of the brain. The motor triggers displayed correspond to leftward turns, a mirror symmetric configuration was also observed for rightward turns (data not shown). The pronounced lateralization of functional types suggests that an

intricate interplay of cross-midline excitation and inhibition is behind the translation of the behavioral turning rates observed in the IPN into locomotor output. Interestingly, ROIs with significant MTNAs are enriched in the telencephalon, which contains among other structures, the homologs of the basal ganglia. In addition, a majority of these ROIs were located in the regions already identified as being of interest in Figures 3.12-3.13, namely the reticular formation and the DRN, suggesting that these regions are involved not only in the integration of sensory evidence, but also the generation of motor output.

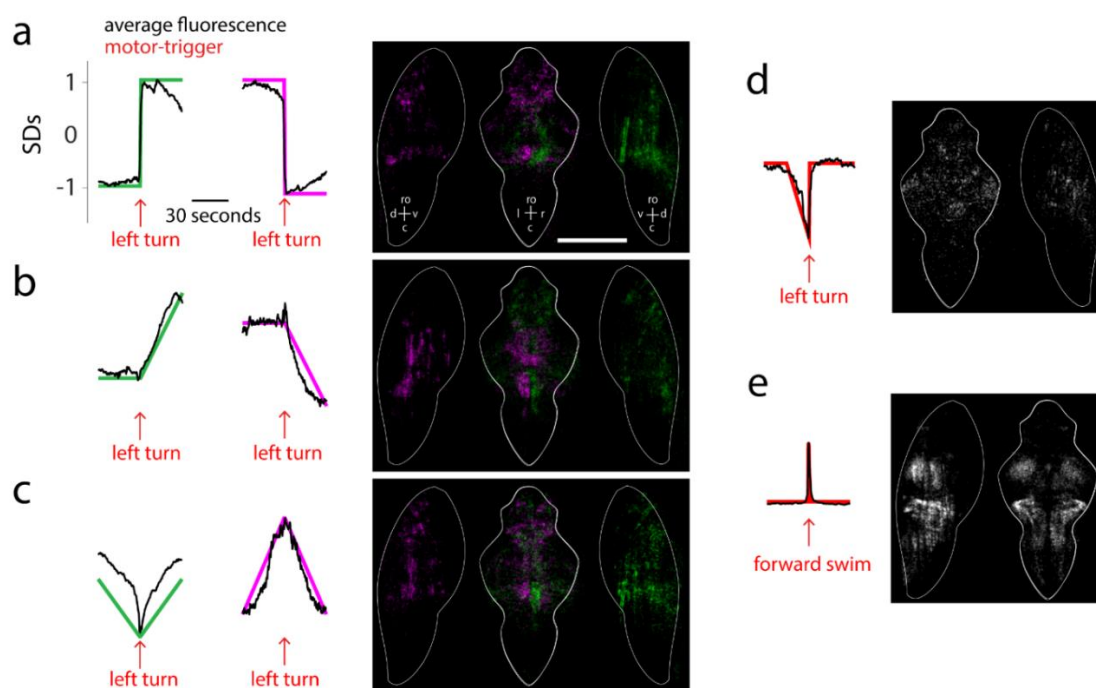


Figure 3.20 Motor-triggered neuronal activity

a. Left: motor triggers corresponding to stepwise increases (green) and decreases (magenta) concurrent with leftward turns. The average activity of all ROIs with correlation > 0.7 with the corresponding motor trigger is superimposed in black. Right: anatomical location of the motor triggers throughout the brain. Ro– rostral, c – caudal, l – left, r – right and scale bar = 300 microns. **b, c.** Similar to **a** but for neuronal activity which ramps up

or down after a left turn (**b**) or neuronal activity which has a maximum or minimum coincident with the left turn (**c**). **d**. Motor trigger corresponding to neuronal activity that decreases steadily and is reset upon a left turn. The number of ROIs with activity that increased steadily and was reset upon a left turn was negligible. **e**. All ROIs with activity coincident with a forward swim. *Figure taken from Dragomir et al. (under review)*

4. Discussion

In this thesis, I present a novel perceptual decision making assay in the larval zebrafish, based on the classic RDM paradigm. Taking advantage of the reflexive OMR, the binary choice of either left or right turning was used as a decision readout, following accumulation of noisy whole field motion. Several behavioral characteristics including latency, turn rate and accuracy were modulated depending on the strength of the visual stimulus, and both sensory and motor history affected the selection of the current behavioral choice. Whole brain functional imaging experiments, combined with an unbiased analysis and modeling approach allowed for a comprehensive identification of almost all neural activity relevant to the various stages of the decision making process and uncovered the IPN as strongly correlating with the turning rate of the fish, potentially deriving from the bidirectional integration of the sensory evidence.

4.1 The OMR as a perceptual decision task

In the classic RDM paradigms used in perceptual decision making studies, there are two phases, the initial one during training or acquisition, and the second proficient one during which testing normally occurs. In this second phase evidence is accumulated and an action is selected irrespective of training: the task becomes one of perceptual decision making in which the integration of sensory evidence is decoupled from any reward signal. The OMR is an innate reflexive behavior: the fish will turn in the direction of perceived motion after integrating incoming sensory evidence without the incentive of an extra reward, therefore this task is analogous to the second proficient phase mentioned above. Additionally, the absence of these reward signals in the OMR makes it easier to isolate the neuronal correlates of pure perceptual decision-making.

The psychometric curves in Figures 3.3b and 3.9 are reminiscent of those obtained in primate perceptual decision making experiments presented with a similar stimulus in either forced-choice or response-time tasks (Gold and Shadlen, 2007) (Figure 1.1b) and indicate that larval zebrafish react to random dot motion stimuli of increasing coherence as motion percepts of increasing strength. Additionally, as the stimulus progresses, the behavior is becoming more robust, both in terms of increased turning rate (Figure 3.3a) as well as turn accuracy (Fig 3.3b and 3.3c), indicating they are accumulating evidence to improve their behavior. In most perceptual decision making assays in primates and rodents, the behavior arises from training aimed to obtaining a reward, after which the accumulation of evidence has no subsequent importance and is automatically reset (Gold and Shadlen, 2007). In contrast, accumulation of evidence is not reset here; one possible interpretation could be that larvae are trying to continuously estimate the state of their visual surroundings to behave accordingly, and evidence accumulated before a bout will still be relevant in estimating the state following the bout. In essence, the external state or evidence variable is encoded in behavioral space as the most appropriate turning rate that should result given current evidence and beliefs.

The freely swimming behavioral analysis indicates that there is a clear dependency to previous sensory stimulus, as well as previous motor choices, a bias that can be extended up to the last 4 motor bouts and their corresponding motion stimulus (Figures 3.5 - 3.7). This is similar to results found by Dunn et al. (2016), which show that in absence of any stimulation, fish do not turn at random, but tend to string together repeated ipsilateral turns before stochastically changing their turning direction. This also connects well with the proposed turn generation stochastic model (Figure 3.16a), where behavioral responses are executed based on a rate that although modulated by evidence, is not updated instantaneously. The history dependence arises because the decision readout mechanism does not reset the integrated evidence, as shown in Figures 3.3c or the inertia-like behavior in Figure 3.5. This effect of sensory and motor history on current choice has also been previously described in several decision making studies in humans, primates and rodents, in paradigms using different sensory modalities (Akrami et al., 2018, Hwang et al, 2017, Fassihi et al., 2014, Gold et al., 2008, Romo and Salinas, 2017).

Swimming in a head fixed preparation is known to occur at a lower rate than in a freely swimming setup (Severi, Portugues et al., 2014; Dunn et al., 2016), and while this is also observed here, turning behavior improves with increased motion coherence in a similar way in both setups (cf. Figures 3.3 and 3.9), validating the use of the head restrained setup in the whole brain functional imaging experiments.

4.2 Neural activity underlying decision making steps

In previous studies, investigation of neural correlates of the decision making process implied a priori knowledge about specific brain areas targeted. These typically focused on parts of the brain involved with preparation and selection of eye movements such as LIP, superior colliculus, FEF (or FOF in rodents), dPFC (Shadlen and Newsome, 1996, 2001; Horwitz and Newsome 1999; Kim and Shadlen 1999; Hanks et al. 2015). Even if the activity recorded here correlated well with accumulated evidence, it remains unclear whether these areas are responsible for this computation, or merely reflect input from different areas. Another limitation was the restricted number of neurons that could be interrogated during a decision task to the potential brain areas involved: in primates, most neurophysiological insights come from single unit recordings, and in rodents, imaging experiments have quite a limited field of view.

This study uses the power of whole brain functional imaging at single cell resolution, which combined with regression analysis and modeling allows for establishing a comprehensive map of all the areas relevant to the various stages of the decision making process. One caveat that is valid in all calcium imaging studies relates to differences in calcium dynamics and calcium indicator concentrations between different neurons, which could result in the different temporal dynamics across the ROIs identified here with both the regression analysis and modeling. While small differences between time constants would indeed be difficult to resolve, their broad distribution, up to tens of seconds (Figure 3.15a), does indicate the presence of both momentary graded and integrated activity patterns in the identified ROIs.

Two main regions emerged from this analysis where sustained and integrated activity in response to different coherences is present: the pretectal/thalamic region and the rostral hindbrain region. The functional model presented in Figure 3.18 proposes that the pretectal/thalamic areas in the diencephalon are more likely to be involved in the visual encoding part of the task while the hindbrain is likely to be directly responsible for turning and swim generation, in agreement with previous findings supporting these roles to these brain regions (Naumann et al., 2016; Dunn et al., 2016; Wolf et al., 2017). This modular architecture could easily accommodate the addition of more turn-inducing stimuli from multiple modalities; the sensory drive, from regions analogous to the pretectum, will then converge onto the same hindbrain turn generator.

The pretectum, the analog of the mammalian nucleus of the optic tract, has been previously described to contain diverse responses to whole-field visual motion in the context of OMR, including monocular, binocular, coherent and conflicting motion, with neurons tuned to a particular direction of the visual motion (Naumann et al., 2016; Kubo et al., 2014). Other studies also indicated the pretectum's contribution to another stabilizing reflex in response to visual motion, the OKR, showing that cells are classified into distinct response profiles, and that many combine inputs from both eyes to process and distinguish between rotational and translational whole-field motion (Kubo et al., 2014; Portugues, Feierstein et al., 2014). These results indicate that different inputs carrying specific characteristics of the visual stimuli converge in the pretectum, and that this area is an important node in the complex sensorimotor transformations underlying visually guided behaviors. Interestingly, this study shows that neurons in the dorsal region of the pretectum are also able to integrate visual sensory drive in time, a feature that has not been previously described.

In addition to activity correlated with directional turning (Figures 3.12 and 3.13), the reticular formation in the anterior hindbrain region showed integrating graded responses that were lateralized depending on visual motion direction, a newly identified response to a region previously known to correlate mostly with motor behavior. This sensory integration response extended from the very rostral region (rhombomere 1) to rhombomeres 2-3, more caudally, which also contained more motor related responses. In absence of any sensory stimulus, Dunn et al. (2016) showed that responses in the more

caudal part of the reticular formation region (which they call the anterior rhombencephalic turning region, ARTR) correlate with direction of turning. Optogenetic perturbations biased swimming direction, while ablation of ARTR resulted in loss of turn bias during the turning history. It would be interesting to investigate whether similar perturbations would likely result in a decreased motor or sensory history effect in this RDM assay, or if optogenetic manipulations would offset the accumulated sensory evidence for turning choice. Wolf et al. (2017) also showed that activity in this hindbrain region (referred to as the hindbrain oscillator) correlated not only with swim bout direction, but also with direction of ocular saccades, linking these behavioral roles to oscillating activity previously found without stimulation or behavioral readout (Ahrens et al., 2013). Swim bout orientation could be reliably predicted by gaze dynamics in the majority of the swim bouts, indicating these distinct motor behaviors could be partly implemented via a common circuit mechanism. In this study, eye movements are not monitored, but it would be interesting to see whether additional behavioral parameters coming from eye movements would help to further explain specific activity patterns observed here. While previous studies focused more on the caudal part of the reticular formation in the hindbrain, not much is known regarding specific neuronal characteristics present in the more rostral part, which concentrates more of the sensory integration responses, or the flow of information between these two subpopulations. Dunn et al. (2016) report the presence of both glutamate and GABA distributed medial-laterally, suggesting the presence of a mutual inhibitory motif underlying the selection of turning direction. Projections to adjacent reticulospinal neurons, which have been shown to be tuned to the specific directionality of the OMR (Orger et al., 2008), could subsequently exert the choice of turn direction onto premotor neurons, but this remains to be tested. Future experiments clarifying neurotransmitter identity in the more rostral hindbrain region as well, together with afferent and efferent projections would further help to identify specific contributions of this area to the choice of turn direction.

Integrating activity graded on coherence magnitude, uni- and bi-directional, was also found in the left dorsal habenula, the zebrafish homolog of the mammalian medial habenula (Amo et al., 2010). The habenulo-IPN pathway has been shown to regulate experience-dependent modification of fear conditioned behavior in zebrafish (Agetsuma

et al., 2010), and in general, the habenula is considered to have an important role in the motivational control of behavior (Hikosaka, 2010). Several studies report responses to ambient light in the left dorsal habenula in zebrafish (Dreosti et al., 2014; Cheng et al., 2017), including a role mediating light preference behavior (Zhang et al., 2017). The RDM assay in this study reveals habenular responses to visual motion, and potential involvement in a perceptual decision task. Responses representing integrating activity to either left or right visual motion, or displaying a bidirectional excitation inhibition pattern (Figure 3.13) were distributed throughout the left dorsal habenula without any particular spatial organization. It is unclear from where these visual inputs arrive, but one possibility would be the bilateral eminentia thalami, which has been shown to relay visual input from retinal ganglion cells to the left dorsal habenula (Zhang et al., 2017), and which also shows neural activity in response to visual motion (Figure 3.10). Similar activity patterns were also observed in the IPN, the main efferent target of the dorsal habenula, where axons terminate in a laterotopic way: left dorsal habenula neurons project mainly to the dorsal and intermediate IPN, while the right dorsal habenula neurons innervate the ventral IPN region (Aizawa et al., 2005; Bianco and Wilson, 2009).

The DRN emerged as another region with multiple types of responses, including uni- and bi-directional integration in response to sensory motion (similar to the habenula and IPN signals), a type of activity not been previously described in this structure. These responses were clustered both along the midline, where the serotonergic cells of the DRN reside, as well as more laterally, overlapping with the GABAergic population. Kawashima et al. (2016) report phasic DRN activity in response to swim-induced visual motion, however, the majority of these neurons did not respond to motion that was not self-generated. They also suggest the involvement of the DRN in motor learning, based on persistent activity following swimming bouts. This type of response is similar to some of the motor correlated responses observed here, where following a swim bout, DRN neurons exhibit a slow rise in activity, which is sustained for up to 3 minutes, before it slowly decays (Figure 3.13, motor output). This activity pattern could be a candidate underlying the motor history effect on behavior, as the observed turning bias can extend to in the order of minutes. Testing this hypothesis with pharmacological ablations or

optogenetic perturbations should help in further elucidating the role of this structure in the turning behavior.

The whole-brain functional screen, together with the modeling approach, uncovered the IPN as a site whose activity strongly correlates with the turning rate of the fish. This nucleus is important integrative center of the limbic system (Morley, 1986), interconnected with the dorsal habenula and the DRN, structures that also contained similar response patterns, and which have been shown to be involved in experience dependent modulation of behavior (Amo et al., 2014, Agetsuma et al., 2010, Chen et al., 2019). The primary input to the IPN comes from the dorsal habenula, which sends axonal projections that wrap multiple times around its center and arborize over a considerable dorsoventral extent (Bianco et al., 2008). Given this particular arrangement, and the fact that the IPN structure itself is composed mostly of neuropil, it is not immediately obvious how the spatially segmented activity pattern presented in Figure 3.19 emerges. Additional inputs come from numerous structures in the brainstem and forebrain, and a wide range of neurotransmitter types are expressed in a spatially organized manner within its subnuclei (Bianco and Wilson, 2009; Morley, 1986), which could contribute to the specific activity pattern observed. Although the left dorsal habenula innervates the dorsal and intermediate pattern of the IPN (Aizawa, 2005), the responses observed here extend to the most ventral planes of the IPN, which should mostly receive input from the right habenula, however, no responses have been identified here that correlate with any of the sensory or motor part of the task. Notably, the IPN has also been implicated in a variety of deficits observed in navigation-based assays in rodents (Sharp et al., 2006; Clark and Taube, 2009). Given its particular circular structure, the fact that activity integrates left and right visual motion as well as reliably tracking directional turning in a stereotyped spatiotemporal profile, certain comparisons can be made with the *Drosophila* ellipsoid body, where navigational cues such as angular path integration and heading are encoded (Seelig and Jayaraman, 2015; Green et al., 2017). Future work on efferent projections should help in elucidating how the directional turning rate encoding units present here relay into motor output.

4.3 Temporal dynamics underlying integrating activity

The imaging analysis together with the integrator model revealed integrating units in multiple clusters of the brain, with a wide range of time constants, which encompass up to tens of seconds. This is comparable with findings from Scott, Constantinople et al. (2017) that show extensive heterogeneity in the dynamics of neuronal responses to sensory stimulation (in the context of a decision making task) in a population of neurons in the frontal and parietal cortex. Neuronal responses could predict the animal's previous and upcoming choice, suggesting influence of sensory and motor history in addition to current sensory variables represented. This was also supported by Akrami et al. (2018), who showed that the current behavioral choice had a substantial sensory history effect, and neural activity in the posterior parietal cortex represented more information about previous-trial sensory stimuli than about current trial stimuli. These findings support a model of evidence accumulation in which a network of heterogeneous neuronal dynamics represents the memory of sensory events during decision-making, as opposed to the typical homogenous dynamics model, in which neurons integrate evidence with a stereotyped temporal waveform representing the latent variable of the accumulator (Scott, Constantinople et al., 2017). This heterogeneous dynamics model underlying sensory history or working memory connects well with the idea of an effective time constant matching behavior that comes from a continuum within a network. This has been previously described in the oculomotor network in the prepositus-vestibular complex neurons (reviewed in Robinson, 1989), which can encode a variety of velocity and position combinations with heterogeneous individual time-constants. These oculomotor integrators of neuronal activity have been well studied in fish (Aksay et al., 2007; Miri et al., 2011; Daie et al., 2015), however, the neuronal activity observed here reflects the temporal integration of external sensory evidence that directly drives behavior and may precede it by many seconds, as opposed to an internally generated efferent signal.

Temporal integration could arise due to cellular biophysical properties, such as specific time constants of the cell membrane or recurrent excitation mediated by NMDA receptor activation, which can account for the slow integration of synaptic inputs (Tank and Hopfield, 1987; Wang, 2002). Regulation of ion channel abundance that leads to

specific membrane voltage dynamic properties has been recently shown to be essential in the integration properties of specific cells involved in an olfactory perception decision task in fruit flies, for example (Groschner, 2018). Alternatively, theoretical models have also demonstrated that integration can be produced from networks with recurrent architecture, which have been proposed to underlie working memory (Major and Tank, 2004; Machens et al., 2005).

4.4 Concluding remarks and future directions

The data presented here indicates that decision-making activity is broadly distributed across different brain regions, underlining the importance of access to whole brain activity in establishing a comprehensive analysis of behavior. Nevertheless, the vast complexity of this whole brain data makes it difficult to outline specific circuit mechanisms regarding the behavior. While this study represents a foundational inquiry into the sensorimotor processing underlying this decision making assay, many open questions remain to be addressed, that will hopefully bolster the proposed model assumptions and shape a functional circuit of the behavior.

In terms of behavior, the freely swimming experiments were performed in a closed loop fashion, such that the direction of visual motion perceived by the fish was always perpendicular to its axis, including right after a turn. This particular construction disregards a potential internal model that would allow the fish to predict the sensory consequences of its own behavior. If such an internal model is present, the sensory reafference experienced by the fish would contradict its predicted sensory feedback, which can result in alterations of the behavior, such as increased latency to turning, or diminished accuracy. Testing the same RDM paradigm in an open loop fashion (allowing the fish to experience the consequences of its directional turning) could help establish whether expected reafference driven by efference copies interferes with the evidence accumulation process and alters certain behavioral parameters. This paradigm can then be extended in the imaging setup as well, and potentially allow for the identification of integrating units that combine sensory evidence with internal efference copy signals.

Testing the effect of the open vs. closed loop scenario could be particularly appropriate to consider in relation to the IPN neural activity representation. Given its particular characteristics that link this structure with potential navigation related properties, it would be interesting to investigate whether motor related cues are integrated together with sensory evidence, as has been shown in the fruit fly ellipsoid body (Seelig and Jayaraman, 2015). This would be further encouraged by previous findings indicating deficits in path integration in a navigational assay following IPN lesions (Clark and Taube, 2009). While the motor triggered analysis (Figure 3.20) also indicates that the IPN is acutely related to motor output, further in depth analysis of motor signals combined with the sensory representation would be required to establish if the specific activity pattern is also altered by motor output, and if both responses contribute to shaping the turning rate observed in behavior.

The generation of motor output model (Figure 3.16) proposes that the IPN reliably encodes behavioral turning rate, through bidirectional integration of sensory evidence. Causal testing of this model could be implemented through optogenetic perturbations or targeted ablations, however, a particular difficulty in targeting this structure stems from its anatomical position: the IPN is located ventrally in the brain, and optogenetic access could be very limited. Employing more advanced techniques such as two-photon holographic optogenetics (dal Maschio et al., 2017) could circumvent this problem, however, this would still require transgenic lines that restrict photostimulation to the neurons of interest. Since the dorsal habenula is the main source of input to the IPN (Morley, 1986) and similar responses have been observed here (in the left dorsal habenula), optogenetic stimulation could also be targeted here, and coupled with calcium imaging to see if these perturbations lead to any changes in the neural activity patterns in the IPN. Evaluating behavior following these perturbations would also be of interest, however, as the habenula has been implicated in several motivation related behavioral modulations (Hikosaka, 2010), the interpretation of these experiments may not be straightforward.

Investigating how a different sensory modality influences neural activity in the IPN, or other regions in the hindbrain likely to be involved in the turning rate representation could further provide support for the proposed generation of motor output model (Figure 3.18). For example, rheotaxis behavior can be induced by non-laminar

water flow around the fish (Oteiza, Odstroil et al., 2017). Titrating the strength of these mechanical stimulations and monitoring neural activity in the IPN or hindbrain areas while fish modulate their turning behavior should indicate whether these structures encode turning rate irrespective of the engaged sensory modality.

The results presented in this thesis provide an exciting perspective into the investigation of brain wide sensorimotor processing underlying a complex behavior, and hopefully future research will further help in unravelling how sensory integration and internal states shape the functional circuits that form behavioral representations and actions.

5. Appendix

5.1 Abbreviations

ARTR	anterior rhombencephalic turning region
dIPFC	dorsolateral prefrontal cortex
dpf	days post fertilization
DRN	dorsal raphe nucleus
IPN	interpeduncular nucleus
FEF	frontal eye field
FFI	feedforward inhibition model
FOF	frontal orienting field
LCA	leaky competing accumulator model
LIP	lateral intraparietal area
MT	medial temporal area
MTNA	motor-triggered neuronal activity averages
nMLF	nucleus of the medial longitudinal fasciculus
NOT	nucleus of the optic tract
OMR	optomotor response
OKR	optokinetic response
PPC	posterior parietal cortex
RDM	random dot motion
SD	standard deviation
SEM	standard error of the mean
SPRT	sequential probability ratio test

5.2 List of figures

Figure 1.1 The RDM paradigm and behavioral characteristics	2
Figure 1.2 LIP firing rates approximate the integral of a difference in firing rate between MT neurons with opposite direction preferences	3
Figure 1.3 Brain regions with response profiles that correlate with accumulating evidence during decision making.....	6
Figure 1.4 Proposed decision making model architectures	7
Figure 1.5 Brain of a 6 dpf zebrafish	10
Figure 1.6 Comprehensive map of brain areas that are active during the OKR behavior.....	12
Figure 2.1 Freely swimming behavioral setup.....	17
Figure 2.2 Schematic of visual motion stimulus.....	18
Figure 2.3 Freely swimming area	18
Figure 3.1 Turning behavior in freely swimming experiments	30
Figure 3.2 Categorization of a turn	31
Figure 3.3 Coherence-dependent turning behavior in freely swimming experiments	32
Figure 3.4 Turning behavior with various stimulus duration	34
Figure 3.5 Turning behavior is dependent on sensory history	36
Figure 3.6 Turning behavior is dependent on motor history	38
Figure 3.7 Sensory and motor history effects on behavior	39
Figure 3.8 Tail tracking and bout categorization in head restrained experiments	41
Figure 3.9 Head restrained turning behavior depending on coherence	42
Figure 3.10 Brain regions sampled during imaging experiments	43
Figure 3.11 Regressors used in whole brain imaging experiments	44
Figure 3.12 Whole-brain ROI maps color coded according to various sensory and motor related regressors	47
Figure 3.13 Neural correlates of the decision making process and their anatomical distribution	48
Figure 3.14 Fitting a general integrator model to the neural data	51
Figure 3.15 Model characteristics and anatomical distribution of fitted ROIs.....	53

Appendix

Figure 3.16 Behavioral predictions of motor output generation model56

Figure 3.17 Relation of turning rate with model fitted fluorescence57

Figure 3.18 Mapping of brain areas to parts of the evidence integration process58

Figure 3.19 Activity in the IPN correlates with the integrated sensory evidence and
directional turning rate59

Figure 3.20 Motor-triggered neuronal activity61

6. References

Agetsuma, M., Aizawa, H., Aoki, T., Nakayama, R., Takahoko, M., Goto, M., Sassa, T., Amo, R., Shiraki, T., Kawakami, K., Hosoya, T., Higashijima, S., Okamoto, H., 2010. The habenula is crucial for experience-dependent modification of fear responses in zebrafish. *Nat Neurosci* 13, 1354–1356. <https://doi.org/10.1038/nn.2654>

Ahrens, M.B., Li, J.M., Orger, M.B., Robson, D.N., Schier, A.F., Engert, F., Portugues, R., 2012. Brain-wide neuronal dynamics during motor adaptation in zebrafish. *Nature* 485, 471–477. <https://doi.org/10.1038/nature11057>

Ahrens, M.B., Orger, M.B., Robson, D.N., Li, J.M., Keller, P.J., 2013. Whole-brain functional imaging at cellular resolution using light-sheet microscopy. *Nature Methods* 10, 413–420. <https://doi.org/10.1038/nmeth.2434>

Aizawa, H., Bianco, I.H., Hamaoka, T., Miyashita, T., Uemura, O., Concha, M.L., Russell, C., Wilson, S.W., Okamoto, H., 2005. Laterotopic Representation of Left-Right Information onto the Dorso-Ventral Axis of a Zebrafish Midbrain Target Nucleus. *Current Biology* 15, 238–243. <https://doi.org/10.1016/j.cub.2005.01.014>

Aizenberg, M., Schuman, E.M., 2011. Cerebellar-Dependent Learning in Larval Zebrafish. *J. Neurosci.* 31, 8708–8712. <https://doi.org/10.1523/JNEUROSCI.6565-10.2011>

Aksay, E., Olasagasti, I., Mensh, B.D., Baker, R., Goldman, M.S., Tank, D.W., 2007. Functional dissection of circuitry in a neural integrator. *Nat Neurosci* 10, 494–504. <https://doi.org/10.1038/nn1877>

Amo, R., Aizawa, H., Takahoko, M., Kobayashi, M., Takahashi, R., Aoki, T., Okamoto, H., 2010. Identification of the Zebrafish Ventral Habenula As a Homolog of the Mammalian Lateral Habenula. *J. Neurosci.* 30, 1566–1574. <https://doi.org/10.1523/JNEUROSCI.3690-09.2010>

Amo, R., Fredes, F., Kinoshita, M., Aoki, R., Aizawa, H., Agetsuma, M., Aoki, T., Shiraki, T., Kakinuma, H., Matsuda, M., Yamazaki, M., Takahoko, M., Tsuboi, T., Higashijima, S., Miyasaka, N., Koide, T., Yabuki, Y., Yoshihara, Y., Fukai, T., Okamoto, H., 2014. The Habenulo-Raphe Serotonergic Circuit Encodes an Aversive Expectation Value Essential for Adaptive Active Avoidance of Danger. *Neuron* 84, 1034–1048. <https://doi.org/10.1016/j.neuron.2014.10.035>

Aoki, T., Kinoshita, M., Aoki, R., Agetsuma, M., Aizawa, H., Yamazaki, M., Takahoko, M., Amo, R., Arata, A., Higashijima, S., Tsuboi, T., Okamoto, H., 2013. Imaging of Neural Ensemble for the Retrieval of a Learned Behavioral Program. *Neuron* 78, 881–894. <https://doi.org/10.1016/j.neuron.2013.04.009>

Bianco, I.H., Carl, M., Russell, C., Clarke, J.D., Wilson, S.W., 2008. Brain asymmetry is encoded at the level of axon terminal morphology. *Neural Development* 3, 9. <https://doi.org/10.1186/1749-8104-3-9>

Bianco, I.H., Kampff, A.R., Engert, F., 2011. Prey Capture Behavior Evoked by Simple Visual Stimuli in Larval Zebrafish. *Front. Syst. Neurosci.* 5. <https://doi.org/10.3389/fnsys.2011.00101>

Bianco, I.H., Wilson, S.W., 2009. The habenular nuclei: a conserved asymmetric relay station in the vertebrate brain. *Philosophical Transactions of the Royal Society B: Biological Sciences* 364, 1005–1020. <https://doi.org/10.1098/rstb.2008.0213>

Bogacz, R., 2007. Optimal decision-making theories: linking neurobiology with behaviour. *Trends in Cognitive Sciences* 11, 118–125. <https://doi.org/10.1016/j.tics.2006.12.006>

Brody, C.D., Hanks, T.D., 2016. Neural underpinnings of the evidence accumulator. *Current Opinion in Neurobiology, Neurobiology of cognitive behavior* 37, 149–157. <https://doi.org/10.1016/j.conb.2016.01.003>

Brunton, B.W., Botvinick, M.M., Brody, C.D., 2013. Rats and Humans Can Optimally Accumulate Evidence for Decision-Making. *Science* 340, 95–98. <https://doi.org/10.1126/science.1233912>

Budick, S.A., O'Malley, D.M., 2000. Locomotor repertoire of the larval zebrafish: swimming, turning and prey capture. *Journal of Experimental Biology* 203, 2565–2579.

Chen, T.-W., Wardill, T.J., Sun, Y., Pulver, S.R., Renninger, S.L., Baohan, A., Schreiter, E.R., Kerr, R.A., Orger, M.B., Jayaraman, V., Looger, L.L., Svoboda, K., Kim, D.S., 2013. Ultrasensitive fluorescent proteins for imaging neuronal activity. *Nature* 499, 295–300. <https://doi.org/10.1038/nature12354>

Chen, W.-Y., Peng, X.-L., Deng, Q.-S., Chen, M.-J., Du, J.-L., Zhang, B.-B., 2019. Role of Olfactorily Responsive Neurons in the Right Dorsal Habenula-Ventral Interpeduncular

Nucleus Pathway in Food-Seeking Behaviors of Larval Zebrafish. *Neuroscience*.
<https://doi.org/10.1016/j.neuroscience.2019.01.057>

Cheng, R.-K., Jesuthasan, S.J., Penney, T.B., 2014. Zebrafish forebrain and temporal conditioning. *Philosophical Transactions of the Royal Society of London B: Biological Sciences* 369, 20120462. <https://doi.org/10.1098/rstb.2012.0462>

Cheng, R.-K., Krishnan, S., Lin, Q., Kibat, C., Jesuthasan, S., 2017. Characterization of a thalamic nucleus mediating habenula responses to changes in ambient illumination. *BMC Biology* 15, 104. <https://doi.org/10.1186/s12915-017-0431-1>

Clark, B.J., Taube, J.S., 2009. Deficits in Landmark Navigation and Path Integration after Lesions of the Interpeduncular Nucleus. *Behav Neurosci* 123, 490–503. <https://doi.org/10.1037/a0015477>

Daie, K., Goldman, M.S., Aksay, E.R.F., 2015. Spatial Patterns of Persistent Neural Activity Vary with the Behavioral Context of Short-Term Memory. *Neuron* 85, 847–860. <https://doi.org/10.1016/j.neuron.2015.01.006>

dal Maschio, M., Donovan, J.C., Helmbrecht, T.O., Baier, H., 2017. Linking Neurons to Network Function and Behavior by Two-Photon Holographic Optogenetics and Volumetric Imaging. *Neuron* 94, 774-789.e5. <https://doi.org/10.1016/j.neuron.2017.04.034>

DasGupta, S., Ferreira, C.H., Miesenböck, G., 2014. FoxP influences the speed and accuracy of a perceptual decision in *Drosophila*. *Science* 344, 901–904. <https://doi.org/10.1126/science.1252114>

Denk, W., Strickler, J.H., Webb, W.W., 1990. Two-photon laser scanning fluorescence microscopy. *Science* 248, 73–76. <https://doi.org/10.1126/science.2321027>

Ding, L., Gold, J.I., 2012. Neural Correlates of Perceptual Decision Making before, during, and after Decision Commitment in Monkey Frontal Eye Field. *Cereb Cortex* 22, 1052–1067. <https://doi.org/10.1093/cercor/bhr178>

Ding, L., Gold, J.I., 2010. Caudate Encodes Multiple Computations for Perceptual Decisions. *J. Neurosci.* 30, 15747–15759. <https://doi.org/10.1523/JNEUROSCI.2894-10.2010>

Ditterich, J., Mazurek, M.E., Shadlen, M.N., 2003. Microstimulation of visual cortex affects the speed of perceptual decisions. *Nature Neuroscience* 6, 891–898. <https://doi.org/10.1038/nn1094>

Douglass, A.D., Kraves, S., Deisseroth, K., Schier, A.F., Engert, F., 2008. Escape Behavior Elicited by Single, Channelrhodopsin-2-Evoked Spikes in Zebrafish Somatosensory Neurons. *Current Biology* 18, 1133–1137. <https://doi.org/10.1016/j.cub.2008.06.077>

Dreosti, E., Vendrell Llopis, N., Carl, M., Yaksi, E., Wilson, S.W., 2014. Left-Right Asymmetry Is Required for the Habenulae to Respond to Both Visual and Olfactory Stimuli. *Current Biology* 24, 440–445. <https://doi.org/10.1016/j.cub.2014.01.016>

Dunn, T.W., Mu, Y., Narayan, S., Randlett, O., Naumann, E.A., Yang, C.-T., Schier, A.F., Freeman, J., Engert, F., Ahrens, M.B., 2016. Brain-wide mapping of neural activity controlling zebrafish exploratory locomotion. *eLife Sciences* 5, e12741. <https://doi.org/10.7554/eLife.12741>

Easter, S.S., Nicola, G.N., 1997. The development of eye movements in the zebrafish (*Danio rerio*). *Developmental Psychobiology* 31, 267–276. [https://doi.org/10.1002/\(SICI\)1098-2302\(199712\)31:4<267::AID-DEV4>3.0.CO;2-P](https://doi.org/10.1002/(SICI)1098-2302(199712)31:4<267::AID-DEV4>3.0.CO;2-P)

Fassihi, A., Akrami, A., Esmaili, V., Diamond, M.E., 2014. Tactile perception and working memory in rats and humans. *PNAS* 111, 2331–2336. <https://doi.org/10.1073/pnas.1315171111>

Feierstein, C.E., Portugues, R., Orger, M.B., 2015. Seeing the whole picture: A comprehensive imaging approach to functional mapping of circuits in behaving zebrafish. *Neuroscience, Contributions from different model organisms to brain research* 296, 26–38. <https://doi.org/10.1016/j.neuroscience.2014.11.046>

Gahtan, E., Tanger, P., Baier, H., 2005. Visual Prey Capture in Larval Zebrafish Is Controlled by Identified Reticulospinal Neurons Downstream of the Tectum. *J. Neurosci.* 25, 9294–9303. <https://doi.org/10.1523/JNEUROSCI.2678-05.2005>

Gold, J.I., Law, C.-T., Connolly, P., Bennur, S., 2008. The Relative Influences of Priors and Sensory Evidence on an Oculomotor Decision Variable During Perceptual Learning. *Journal of Neurophysiology* 100, 2653–2668. <https://doi.org/10.1152/jn.90629.2008>

Gold, J.I., Shadlen, M.N., 2007. The Neural Basis of Decision Making. *Annual Review of Neuroscience* 30, 535–574. <https://doi.org/10.1146/annurev.neuro.29.051605.113038>

Gold, J.I., Shadlen, M.N., 2003. The Influence of Behavioral Context on the Representation of a Perceptual Decision in Developing Oculomotor Commands. *J. Neurosci.* 23, 632–651. <https://doi.org/10.1523/JNEUROSCI.23-02-00632.2003>

Gold, J.I., Shadlen, M.N., 2000. Representation of a perceptual decision in developing oculomotor commands. *Nature* 404, 390–394. <https://doi.org/10.1038/35006062>

Green, J., Adachi, A., Shah, K.K., Hirokawa, J.D., Magani, P.S., Maimon, G., 2017. A neural circuit architecture for angular integration in *Drosophila*. *Nature* 546, 101–106. <https://doi.org/10.1038/nature22343>

Groschner, L.N., Chan Wah Hak, L., Bogacz, R., DasGupta, S., Miesenböck, G., 2018. Dendritic Integration of Sensory Evidence in Perceptual Decision-Making. *Cell* 173, 894–905.e13. <https://doi.org/10.1016/j.cell.2018.03.075>

Hanes, D.P., Schall, J.D., 1996. Neural Control of Voluntary Movement Initiation. *Science* 274, 427–430. <https://doi.org/10.1126/science.274.5286.427>

Hanks, T.D., Ditterich, J., Shadlen, M.N., 2006. Microstimulation of macaque area LIP affects decision-making in a motion discrimination task. *Nature Neuroscience* 9, 682–689. <https://doi.org/10.1038/nn1683>

Hanks, T.D., Kopec, C.D., Brunton, B.W., Duan, C.A., Erlich, J.C., Brody, C.D., 2015. Distinct relationships of parietal and prefrontal cortices to evidence accumulation. *Nature* 520, 220–223. <https://doi.org/10.1038/nature14066>

Hikosaka, O., 2010. The habenula: from stress evasion to value-based decision-making. *Nat Rev Neurosci* 11, 503–513. <https://doi.org/10.1038/nrn2866>

Horwitz, G.D., Newsome, W.T., 2001. Target Selection for Saccadic Eye Movements: Direction-Selective Visual Responses in the Superior Colliculus. *Journal of Neurophysiology* 86, 2527–2542.

Horwitz, G.D., Newsome, W.T., 1999. Separate Signals for Target Selection and Movement Specification in the Superior Colliculus. *Science* 284, 1158–1161. <https://doi.org/10.1126/science.284.5417.1158>

Huang, K.-H., Ahrens, M.B., Dunn, T.W., Engert, F., 2013. Spinal Projection Neurons Control Turning Behaviors in Zebrafish. *Current Biology* 23, 1566–1573. <https://doi.org/10.1016/j.cub.2013.06.044>

Hwang, E.J., Dahlen, J.E., Mukundan, M., Komiyama, T., 2017. History-based action selection bias in posterior parietal cortex. *Nature Communications* 8, 1242. <https://doi.org/10.1038/s41467-017-01356-z>

Katz, L.N., Yates, J.L., Pillow, J.W., Huk, A.C., 2016. Dissociated functional significance of decision-related activity in the primate dorsal stream. *Nature* 535, 285–288. <https://doi.org/10.1038/nature18617>

Kawashima, T., Zwart, M.F., Yang, C.-T., Mensh, B.D., Ahrens, M.B., 2016. The Serotonergic System Tracks the Outcomes of Actions to Mediate Short-Term Motor Learning. *Cell* 167, 933-946.e20. <https://doi.org/10.1016/j.cell.2016.09.055>

Kerr, J.N.D., Denk, W., 2008. Imaging in vivo: watching the brain in action. *Nature Reviews Neuroscience* 9, 195–205. <https://doi.org/10.1038/nrn2338>

Kim, D.H., Kim, J., Marques, J.C., Grama, A., Hildebrand, D.G.C., Gu, W., Li, J.M., Robson, D.N., 2017. Pan-neuronal calcium imaging with cellular resolution in freely swimming zebrafish. *Nature Methods* 14, 1107–1114. <https://doi.org/10.1038/nmeth.4429>

Kim, J.-N., Shadlen, M.N., 1999. Neural correlates of a decision in the dorsolateral prefrontal cortex of the macaque. *Nat Neurosci* 2, 176–185. <https://doi.org/10.1038/5739>

Knogler, L.D., Kist, A.M., Portugues, R., n.d. Motor context dominates output from purkinje cell functional regions during reflexive visuomotor behaviours. *eLife* 8. <https://doi.org/10.7554/eLife.42138>

Kubo, F., Hablitzel, B., Dal Maschio, M., Driever, W., Baier, H., Arrenberg, A.B., 2014. Functional Architecture of an Optic Flow-Responsive Area that Drives Horizontal Eye Movements in Zebrafish. *Neuron* 81, 1344–1359. <https://doi.org/10.1016/j.neuron.2014.02.043>

Laming, D.R.J., 1968. Information theory of choice-reaction times, Information theory of choice-reaction times. Academic Press, Oxford, England.

Licata, A.M., Kaufman, M.T., Raposo, D., Ryan, M.B., Sheppard, J.P., Churchland, A.K., 2017. Posterior Parietal Cortex Guides Visual Decisions in Rats. *J. Neurosci.* 37, 4954–4966. <https://doi.org/10.1523/JNEUROSCI.0105-17.2017>

Liu, K.S., Fetcho, J.R., 1999. Laser Ablations Reveal Functional Relationships of Segmental Hindbrain Neurons in Zebrafish. *Neuron* 23, 325–335. [https://doi.org/10.1016/S0896-6273\(00\)80783-7](https://doi.org/10.1016/S0896-6273(00)80783-7)

Maaswinkel, H., Li, L., 2003. Spatio-temporal frequency characteristics of the optomotor response in zebrafish. *Vision Research* 43, 21–30. [https://doi.org/10.1016/S0042-6989\(02\)00395-4](https://doi.org/10.1016/S0042-6989(02)00395-4)

Machens, C.K., Romo, R., Brody, C.D., 2005. Flexible Control of Mutual Inhibition: A Neural Model of Two-Interval Discrimination. *Science* 307, 1121–1124. <https://doi.org/10.1126/science.1104171>

Major, G., Tank, D., 2004. Persistent neural activity: prevalence and mechanisms. *Current Opinion in Neurobiology* 14, 675–684. <https://doi.org/10.1016/j.conb.2004.10.017>

Mante, V., Sussillo, D., Shenoy, K.V., Newsome, W.T., 2013. Context-dependent computation by recurrent dynamics in prefrontal cortex. *Nature* 503, 78–84. <https://doi.org/10.1038/nature12742>

Mazurek, M.E., Roitman, J.D., Ditterich, J., Shadlen, M.N., 2003. A role for neural integrators in perceptual decision making. *Cereb. Cortex* 13, 1257–1269.

Miri, A., Daie, K., Arrenberg, A.B., Baier, H., Aksay, E., Tank, D.W., 2011. Spatial gradients and multidimensional dynamics in a neural integrator circuit. *Nat Neurosci* 14, 1150–1159. <https://doi.org/10.1038/nn.2888>

Morley, B.J., 1986. The Interpeduncular Nucleus, in: *International Review of Neurobiology*. Elsevier, pp. 157–182. [https://doi.org/10.1016/S0074-7742\(08\)60108-7](https://doi.org/10.1016/S0074-7742(08)60108-7)

Mueller, T., Wullimann, M., 2016. *Atlas of Early Zebrafish Brain Development*. Elsevier 2nd Edition. <https://doi.org/10.1016/C2013-0-00639-1>

Naumann, E.A., Fitzgerald, J.E., Dunn, T.W., Rihel, J., Sompolinsky, H., Engert, F., 2016. From Whole-Brain Data to Functional Circuit Models: The Zebrafish Optomotor Response. *Cell* 167, 947-960.e20. <https://doi.org/10.1016/j.cell.2016.10.019>

Naumann, E.A., Kampff, A.R., Prober, D.A., Schier, A.F., Engert, F., 2010. Monitoring neural activity with bioluminescence during natural behavior. *Nature Neuroscience* 13, 513–520. <https://doi.org/10.1038/nn.2518>

Neuhauss, S.C.F., Biehlmaier, O., Seeliger, M.W., Das, T., Kohler, K., Harris, W.A., Baier, H., 1999. Genetic Disorders of Vision Revealed by a Behavioral Screen of 400 Essential Loci in Zebrafish. *J. Neurosci.* 19, 8603–8615. <https://doi.org/10.1523/JNEUROSCI.19-19-08603.1999>

Newsome, W.T., Britten, K.H., Movshon, J.A., 1989. Neuronal correlates of a perceptual decision. *Nature* 341, 52–54. <https://doi.org/10.1038/341052a0>

Newsome, W.T., Pare, E.B., 1988. A selective impairment of motion perception following lesions of the middle temporal visual area (MT). *J. Neurosci.* 8, 2201–2211. <https://doi.org/10.1523/JNEUROSCI.08-06-02201.1988>

O’Connell, R.G., Dockree, P.M., Kelly, S.P., 2012. A supramodal accumulation-to-bound signal that determines perceptual decisions in humans. *Nature Neuroscience* 15, 1729–1735. <https://doi.org/10.1038/nn.3248>

Optim: A mathematical optimization package for Julia [WWW Document], 2018. . The Journal of Open Source Software. <https://doi.org/10.21105/joss.00615>

Orger, M.B., Kampff, A.R., Severi, K.E., Bollmann, J.H., Engert, F., 2008. Control of visually guided behavior by distinct populations of spinal projection neurons. *Nat Neurosci* 11, 327–333. <https://doi.org/10.1038/nn2048>

Orger, M.B., Smear, M.C., Anstis, S.M., Baier, H., 2000. Perception of Fourier and non-Fourier motion by larval zebrafish. *Nature Neuroscience* 3, 1128–1133. <https://doi.org/10.1038/80649>

Oteiza, P., Odstrcil, I., Lauder, G., Portugues, R., Engert, F., 2017. A novel mechanism for mechanosensory-based rheotaxis in larval zebrafish. *Nature* 547, 445–448. <https://doi.org/10.1038/nature23014>

Panier, T., Romano, S., Olive, R., Pietri, T., Sumbre, G., Candelier, R., Debrégeas, G., 2013. Fast functional imaging of multiple brain regions in intact zebrafish larvae using Selective Plane Illumination Microscopy. *Front. Neural Circuits* 7. <https://doi.org/10.3389/fncir.2013.00065>

Portugues, R., Engert, F., 2011. Adaptive Locomotor Behavior in Larval Zebrafish. *Front. Syst. Neurosci.* 5. <https://doi.org/10.3389/fnsys.2011.00072>

Portugues, R., Engert, F., 2009. The neural basis of visual behaviors in the larval zebrafish. *Current Opinion in Neurobiology, Motor systems • Neurology of behaviour* 19, 644–647. <https://doi.org/10.1016/j.conb.2009.10.007>

Portugues, R., Feierstein, C.E., Engert, F., Orger, M.B., 2014. Whole-Brain Activity Maps Reveal Stereotyped, Distributed Networks for Visuomotor Behavior. *Neuron* 81, 1328–1343. <https://doi.org/10.1016/j.neuron.2014.01.019>

Portugues, R., Haesemeyer, M., Blum, M.L., Engert, F., 2015. Whole-field visual motion drives swimming in larval zebrafish via a stochastic process. *Journal of Experimental Biology* 218, 1433–1443. <https://doi.org/10.1242/jeb.118299>

Portugues, R., Severi, K.E., Wyart, C., Ahrens, M.B., 2013. Optogenetics in a transparent animal: circuit function in the larval zebrafish. *Current Opinion in Neurobiology, Neurogenetics* 23, 119–126. <https://doi.org/10.1016/j.conb.2012.11.001>

Ratcliff, R., 1978. A theory of memory retrieval. *Psychological Review* 85, 59–108. <https://doi.org/10.1037/0033-295X.85.2.59>

Ratcliff, R., Cheria, A., Segraves, M., 2003. A Comparison of Macaque Behavior and Superior Colliculus Neuronal Activity to Predictions From Models of Two-Choice Decisions. *Journal of Neurophysiology* 90, 1392–1407. <https://doi.org/10.1152/jn.01049.2002>

Ratcliff, R., Smith, P.L., 2004. A Comparison of Sequential Sampling Models for Two-Choice Reaction Time. *Psychological Review* 111, 333–367. <https://doi.org/10.1037/0033-295X.111.2.333>

Robinson, D.A., 1989. Integrating with Neurons. *Annual Review of Neuroscience* 12, 33–45. <https://doi.org/10.1146/annurev.ne.12.030189.000341>

Roeser, T., Baier, H., 2003. Visuomotor Behaviors in Larval Zebrafish after GFP-Guided Laser Ablation of the Optic Tectum. *J. Neurosci.* 23, 3726–3734. <https://doi.org/10.1523/JNEUROSCI.23-09-03726.2003>

Rohlfing, T., Maurer, C.R., 2003. Nonrigid image registration in shared-memory multiprocessor environments with application to brains, breasts, and bees. *IEEE Trans Inf Technol Biomed* 7, 16–25.

Roitman, J.D., Shadlen, M.N., 2002. Response of Neurons in the Lateral Intraparietal Area during a Combined Visual Discrimination Reaction Time Task. *J. Neurosci.* 22, 9475–9489.

Romo, R., Salinas, E., 2003. Cognitive neuroscience: Flutter Discrimination: neural codes, perception, memory and decision making. *Nature Reviews Neuroscience* 4, 203–218. <https://doi.org/10.1038/nrn1058>

Salzman, C.D., Britten, K.H., Newsome, W.T., 1990. Cortical microstimulation influences perceptual judgements of motion direction. *Nature* 346, 174–177. <https://doi.org/10.1038/346174a0>

Schoonheim, P.J., Arrenberg, A.B., Bene, F.D., Baier, H., 2010. Optogenetic Localization and Genetic Perturbation of Saccade-Generating Neurons in Zebrafish. *J. Neurosci.* 30, 7111–7120. <https://doi.org/10.1523/JNEUROSCI.5193-09.2010>

Scott, B.B., Constantinople, C.M., Akrami, A., Hanks, T.D., Brody, C.D., Tank, D.W., 2017. Fronto-parietal Cortical Circuits Encode Accumulated Evidence with a Diversity of Timescales. *Neuron* 0. <https://doi.org/10.1016/j.neuron.2017.06.013>

Scott, E.K., Mason, L., Arrenberg, A.B., Ziv, L., Gosse, N.J., Xiao, T., Chi, N.C., Asakawa, K., Kawakami, K., Baier, H., 2007. Targeting neural circuitry in zebrafish using GAL4 enhancer trapping. *Nature Methods* 4, 323–326. <https://doi.org/10.1038/nmeth1033>

Severi, K.E., Portugues, R., Marques, J.C., O'Malley, D.M., Orger, M.B., Engert, F., 2014. Neural control and modulation of swimming speed in the larval zebrafish. *Neuron* 83, 692–707. <https://doi.org/10.1016/j.neuron.2014.06.032>

Shadlen, M.N., Newsome, W.T., 2001. Neural Basis of a Perceptual Decision in the Parietal Cortex (Area LIP) of the Rhesus Monkey. *Journal of Neurophysiology* 86, 1916–1936. <https://doi.org/10.1152/jn.2001.86.4.1916>

Shadlen, M.N., Newsome, W.T., 1996. Motion perception: seeing and deciding. *PNAS* 93, 628–633. <https://doi.org/10.1073/pnas.93.2.628>

- Sharp, P.E., Turner-Williams, S., Tuttle, S., 2006. Movement-related correlates of single cell activity in the interpeduncular nucleus and habenula of the rat during a pellet-chasing task. *Behavioural Brain Research* 166, 55–70. <https://doi.org/10.1016/j.bbr.2005.07.004>
- Smith, P.L., Ratcliff, R., 2004. Psychology and neurobiology of simple decisions. *Trends in Neurosciences* 27, 161–168. <https://doi.org/10.1016/j.tins.2004.01.006>
- Štih, V., Petrucco, L., Kist, A.M., Portugues, R., 2018. Stytra: an open-source, integrated system for stimulation, tracking and closed-loop behavioral experiments. *bioRxiv* 492553. <https://doi.org/10.1101/492553>
- Stone, M., 1960. Models for choice-reaction time. *Psychometrika* 25, 251–260. <https://doi.org/10.1007/BF02289729>
- Suster, M.L., Kikuta, H., Urasaki, A., Asakawa, K., Kawakami, K., 2009. Transgenesis in Zebrafish with the Tol2 Transposon System, in: Cartwright, E.J. (Ed.), *Transgenesis Techniques: Principles and Protocols, Methods in Molecular Biology*. Humana Press, Totowa, NJ, pp. 41–63. https://doi.org/10.1007/978-1-60327-019-9_3
- Tank, D.W., Hopfield, J.J., 1987. Neural computation by concentrating information in time. *PNAS* 84, 1896–1900. <https://doi.org/10.1073/pnas.84.7.1896>
- Teodorescu, A.R., Usher, M., 2013. Disentangling decision models: From independence to competition. *Psychological Review* 120, 1–38. <https://doi.org/10.1037/a0030776>
- Thiele, T.R., Donovan, J.C., Baier, H., 2014. Descending Control of Swim Posture by a Midbrain Nucleus in Zebrafish. *Neuron* 83, 679–691. <https://doi.org/10.1016/j.neuron.2014.04.018>
- Usher, M., McClelland, J.L., 2001. The time course of perceptual choice: The leaky, competing accumulator model. *Psychological Review* 108, 550–592. <https://doi.org/10.1037/0033-295X.108.3.550>
- Vickers, D., 1970. Evidence for an Accumulator Model of Psychophysical Discrimination. *Ergonomics* 13, 37–58. <https://doi.org/10.1080/00140137008931117>
- Wald, A., Wolfowitz, J., 1950. Bayes Solutions of Sequential Decision Problems. *Ann. Math. Statist.* 21, 82–99. <https://doi.org/10.1214/aoms/1177729887>
- Wang, X.-J., 2002. Probabilistic Decision Making by Slow Reverberation in Cortical Circuits. *Neuron* 36, 955–968. [https://doi.org/10.1016/S0896-6273\(02\)01092-9](https://doi.org/10.1016/S0896-6273(02)01092-9)

Wolf, S., Dubreuil, A.M., Bertoni, T., Böhm, U.L., Bormuth, V., Candelier, R., Karpenko, S., Hildebrand, D.G.C., Bianco, I.H., Monasson, R., Debrégeas, G., 2017. Sensorimotor computation underlying phototaxis in zebrafish. *Nature Communications* 8, 651. <https://doi.org/10.1038/s41467-017-00310-3>

Wyart, V., de Gardelle, V., Scholl, J., Summerfield, C., 2012. Rhythmic Fluctuations in Evidence Accumulation during Decision Making in the Human Brain. *Neuron* 76, 847–858. <https://doi.org/10.1016/j.neuron.2012.09.015>

Yartsev, M.M., Hanks, T.D., Yoon, A.M., Brody, C.D., 2018. Causal contribution and dynamical encoding in the striatum during evidence accumulation. *eLife* 7, e34929. <https://doi.org/10.7554/eLife.34929>

Zhang, B., Yao, Y., Zhang, H., Kawakami, K., Du, J., 2017. Left Habenula Mediates Light-Preference Behavior in Zebrafish via an Asymmetrical Visual Pathway. *Neuron* 93, 914–928.e4. <https://doi.org/10.1016/j.neuron.2017.01.011>

List of publications

Dragomir, E.I., Štih, V., Portugues, R. *Evidence accumulation during a perceptual decision task revealed by whole-brain imaging* (Nature Neuroscience, under review)

Knogler, L.D., Markov, D., **Dragomir, E.I., Štih, V., Portugues, R.** *Sensorimotor Representations in Cerebellar Granule Cells in Larval Zebrafish Are Dense, Spatially Organized, and Non-temporally Patterned.* Current Biology (2017)

Acknowledgments

I am very grateful to my PhD supervisor, Ruben Portugues, for all the support and help throughout my PhD experience. Thank you Ruben, first of all for taking me in the lab (even if I forced myself in), for all your kindness and patience, constant faith in me, for being an excellent scientific mentor and teacher, for always finding ways to keep my motivation high.

Thanks to all the wonderful members of the Portugues Lab, for all their help and sharing great times in the lab, that also helped to sweeten the tough times. Thanks to Vilim, who also helped a lot with my PhD project.

I would also like to thank Nadine Gogolla and Axel Borst, for giving me insightful advice throughout my PhD project.

I am grateful to GSN for providing me with the chance of doing my PhD and for all their support and help.

Thanks to all the GSN-derived friends, with whom I have shared great moments, and who helped balance the difficult moments of the PhD with times filled with laughter.

Thank you Julian, for all your care and kindness.

Thank you Cipri, for all your support and trust in me.

I would not have made it this far without the support of my parents, who always strived to provide me with all the opportunities possible, and helped me grow into the person I am today. Thank you for everything.

Eidesstattliche Versicherung/Affidavit

Hiermit versichere ich an Eides statt, dass ich die vorliegende Dissertation „*Perceptual decision making in larval zebrafish revealed by whole-brain imaging*“ selbstständig angefertigt habe, mich außer der angegebenen keiner weiteren Hilfsmittel bedient und alle Erkenntnisse, die aus dem Schrifttum ganz oder annähernd übernommen sind, als solche kenntlich gemacht und nach ihrer Herkunft unter Bezeichnung der Fundstelle einzeln nachgewiesen habe.

I hereby confirm that the dissertation “*Perceptual decision making in larval zebrafish revealed by whole-brain imaging*” is the result of my own work and that I have only used sources or materials listed and specified in the dissertation.

München, den 12. März/Munich, March 12th

Unterschrift/signature

Elena Dragomir

Declaration of author contributions

Elena I. Dragomir and Ruben Portugues conceived the project and designed the experiments.

Elena I. Dragomir performed all experiments.

Elena I. Dragomir and Ruben Portugues analyzed experimental data.

Vilim Štíh and Ruben Portugues designed and implemented the generalized integrator model and stochastic turn generator model, with input from Elena I. Dragomir.